EFFECT OF ALLOYING ADDITIONS OF ALUMINIUM AND IRON ON THE CREEP RESISTANCE OF TI-12CR (WT.%)

By

Harish Narasimhan Chakravarty

A THESIS

Submitted to
Michigan State University
in partial fulfillment of the requirements
for the degree of

Materials Science and Engineering-Master of Science

2019

ABSTRACT

EFFECT OF ALLOYING ADDITIONS OF ALUMINIUM AND IRON ON THE CREEP RESISTANCE OF TI-12CR (WT.%)

By

Harish Narasimhan Chakravarty

Titanium (Ti) and its alloys are among the desired materials for biomaterial, marine, and aerospace applications due to their excellent properties. Metastable beta titanium (β-Ti) alloys exhibit enhanced strengths and hardness values after thermomechanical processing (TMP) due to the presence of omega (ω) and alpha (α) phase precipitates in the beta (β) matrix. Cost is a major driving factor in titanium research. There have been significant efforts to replace high cost alloying elements currently being used in the industry, like V, Sn, Mo, Nb, and Zr, with cheaper ferro-chrome substitutes. The goal going forward for metastable β-Ti alloys is achieving comparable mechanical properties to the commercially used Ti-alloys. β-Ti alloys with the ω-phase usually tend to exhibit higher strengths and hardness values than the ones that do not contain the ω-phase.

In this study, the creep properties of three different β-Ti alloys, Ti-12Cr-1Fe-3Al (wt. %), Ti-12Cr-3Al (wt.%), and T-12Cr (wt. %), were experimentally obtained at a temperature of 683K and applied stresses between 200-350 MPa. The relationship between microstructure and creep properties were investigated. X-ray diffractometer (XRD), optical microscope (OM), and scanning electron microscope (SEM) were used to help characterize the microstructure before and after creep deformation. The hardness of alloys increased after heat treatment for 48 hrs at 683 K due to the precipitation of the α and/or the ω phases. The creep tests showed that Ti-12Cr-1Fe-3Al (wt. %) was the most creep resistant and Ti-12Cr (wt. %) was the least creep resistant

ACKNOWLEDGEMENTS

First, I would like to sincerely thank my advisor, Dr. Carl Boehlert, for having given me this opportunity to be a part of his research group. He has constantly guided and supported me in my master's work and has always been available to discuss and resolve any technical aspects of my research. As a person, he was always a friend to me and has shown great care and understanding, which has made my time here at MSU a wonderful one.

I would like to thank my professors, Dr. Alex Zevalkink, Dr. Nathan Mellott, Dr. Wei Lai, Dr. Eisenlohr, for helping me understand various aspects of materials science and providing me with a strong foundation for my research work. I would like to thank the current and former members of the "metals group", who have directly and indirectly helped me in my research work. I would like to thank Prof. Masahiko Ikeda for providing the materials used in this research study.

I would like to specially thank JoAnn Ballor for all her help in the lab, especially with polishing samples. I'm also grateful to Geeta Kumari and David Hernandez Escobar for their help in various aspects of my research work, and their support as colleagues and friends. I would like to thank Per Askeland for his help in working with the scanning electron microscope.

I'm deeply indebted to my parents for their selfless love, support, and their constant belief in me. I would be remiss if I didn't thank my friends, Srivalli Dingari, Animesh Krishna, Rajat Verma, Swapna Sindhu Mishra, Bansari Chauhan, Aishwarya Bhatlawande, and Kshitija Deshmukh, for constantly being there for me, and making me feel at home away from home. Cheers to all of you. I would like to finally thank my family and my cousins: Arjun, Anand, Deepika, Navya and Krishna for their support and faith in me.

TABLE OF CONTENTS

LIST OF TABLES

LIST OF FIGURES

KEY TO SYMBOLS AND ABBREVIATIONS

3D Three-dimensional

Al Aluminum

ASTM American society for testing and materials

bcc Body-centered cubic

BSE Backscattered electron

CP Commercially pure

Cr Chromium

Cu Copper

EBSD Electron backscattered diffraction

EDM Electrical discharge machining

ε_f elongation-to-failure

$\varepsilon_{ssmin}/\dot{\varepsilon}/\varepsilon_{aa}$ Steady state strain

Fe Iron

fcc Face centered cubic

hcp Hexagonal closed-packed

Mg Magnesium

Mo Molybdenum

n creep/stress exponent

N Nitrogen

Nb Niobium

Ni Nickel

RT Room temperature

O   Oxygen

σ stress

SE   Secondary electron

SEM   Scanning electron microscopy

SiC   Silicon carbide

TEM   Transmission electron microscopy

Ti   Titanium

V   Vanadium

wt.%   Weight percent

XRD   X-ray diffraction

Zr   Zirconium

TC   Ti-12Cr-1Fe-3Al

TCA   Ti-12Cr-3Al

TCFA   Ti-12Cr-1Fe-3A

CHAPTER 1

INTRODUCTION, BACKGROUND, AND MOTIVATION

1.1 Rationale and Research objective

Ti and its alloys have been commercially used for over 50 years and have made significant contributions to many fields such as aerospace, chemical plant, oil and gas, marine, thermal, and nuclear power stations. The principle strengths of Ti compared to other structural metallic metals based on iron (Fe), nickel (Ni), aluminum (Al), and magnesium (Mg), are its high specific strength (high strength and low density), excellent corrosion resistance, and the capacity to withstand extreme temperatures (Leyens and Peters, 2003a). Table 1.1 summarizes some of the important characteristic of Ti and its alloys with other commonly used structural alloys.

Table 1. 1 Important characteristics of Ti and Ti based alloys as compared to other structural metallic materials based on Fe, Ni, Al, and Mg (G Lütjering and Williams, 2003)

	Ti	**Fe**	**Ni**	**Al**
Melting Temperature (°C)	1670	1538	1455	660
RT E (GPa)	115	215	200	72
Yield Stress Level (MPa)	1000	1000	1000	1000
Density (g/cm3)	4.5	7.9	8.9	2.7
Comparative Corrosion Resistance	Very High	Low	Medium	High
Comparative Reactivity with Oxygen	Very High	Low	Low	High
Comparative Price of Metal	Very High	Low	High	Medium

About 80% of Ti production is for aviation and aerospace industry. Approximately 21% of B-1 bomber's body structure material is Ti, mainly for the manufacture of the fuselage, wings, skins and load-bearing component (Chunxiang *et al.*, 2011). In the F-15 fighter structural materials, Ti-alloys occupy a capacity of 7000 kg, which is about 34% structural weight of the airframe. For Boeing 757 aircraft the structural weight percentage is 5%. And as for DC10 aircraft produced by McDonnell Douglas, Ti-alloys accounts for more than 10% of its structural weight (Liu *et al.*, 2008). Figure 1.1 shows an example of F-22 military aircraft wing fitting made from Ti-alloys.

Figure 1. 1 Cast Ti-6Al-4V wing attach fitting for the F-22 military aircraft (Lütjering, G., and Williams, 2003).

Ti and its alloys are superior to many materials such as stainless and pyrolytic carbon in terms of mechanical properties and biocompatibility. They are widely used in biomedical devices and components especially as hard tissue replacements because of their desirable properties, such as relatively low modulus, good fatigue strength, corrosion resistance, and biocompatibility. One of the most common applications of Ti and its alloys is in artificial hip joints that consist of an articulating bearing (femoral head and cup) and stem as depicted in Figure 1.2 (Chunxiang *et al.*, 2003, 2011).

Figure 1. 2 Schematic diagram of artificial hip implant (Chunxiang et al., 2003)

Cost is a major driving factor in Ti research. Processing Ti from its naturally occurring oxide state is expensive due to inert atmosphere requirements and post-processing costs. Figure 1.3 shows the US producer price index for finished rolled titanium (Producer Price Index, PPI) changes during 1971–2006 years (Ivasyshyn and Aleksandrov, 2008). Replacing commonly used alloying elements like vanadium (V), niobium (Nb), and molybdenum (Mo) with lower cost alternatives like Chromium (Cr) and Iron (Fe) is a potential means to reduce the costs (Cotton *et al.*, 2015).

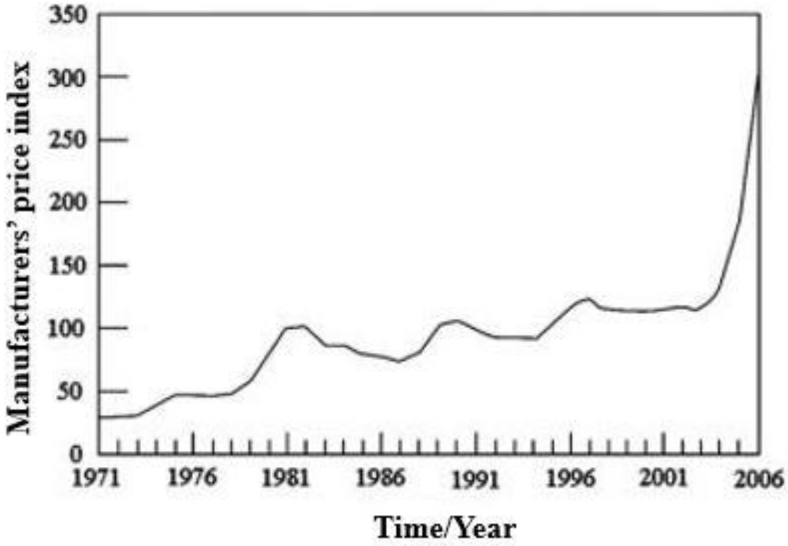

Figure 1. 3 Producer/Manufacturers' price index for finished rolled Ti in the US between 1971-2006 (Chunxiang et al., 2011).

As Ti and its alloys are often used in critical applications and it becomes essential to thoroughly understand their mechanical properties and deformation behavior. Also, Ti-alloys, being relatively newer materials compared to steel or Al, it is imperative to obtain a detailed characterization of their microstructures and mechanical properties. J. Ballor et al. studied microstructure-property relationships of four Ti-12Cr (wt. %) alloys and the effect of individual alloying elements was investigated (J. Ballor *et al.*, 2019). This thesis study was intended to further the understanding of the mechanical properties of the same alloys.

1.2 Fundamental of Ti and Ti alloys

1.2.1 Crystal structure

Ti is a transition metal belonging to the IV-A group in the periodic table with an atomic number of 22, atomic weight of 47.88, and has the low temperature equilibrium phase with hexagonal crystal structure designated as α (a = 0.295nm, c = 0.468nm, c/a = 1.587 (at 298 K)). Ti is allotropic and exhibits more than one crystal structure. At 1155 K, the hcp α-phase transforms to the high temperature bcc β-phase (a = 0.3307nm (1173K)). Apart from the equilibrium phases, Ti alloys also exhibit non-equilibrium phases such as orthorhombic martensite (α''), ω-phase, retained β-phase and β'-phase (Leyens and Peters, 2003b; Lütjering, G., and Williams, 2003). Figure 1.4 represents schematic unit cells of α, β, and ω phases for pure Ti, and the corresponding lattice parameters are provided in Table 1.1 (Hickman, 1969; Welsch, Boyer and Collings, 1993; Gerd Lütjering and Williams, 2003).

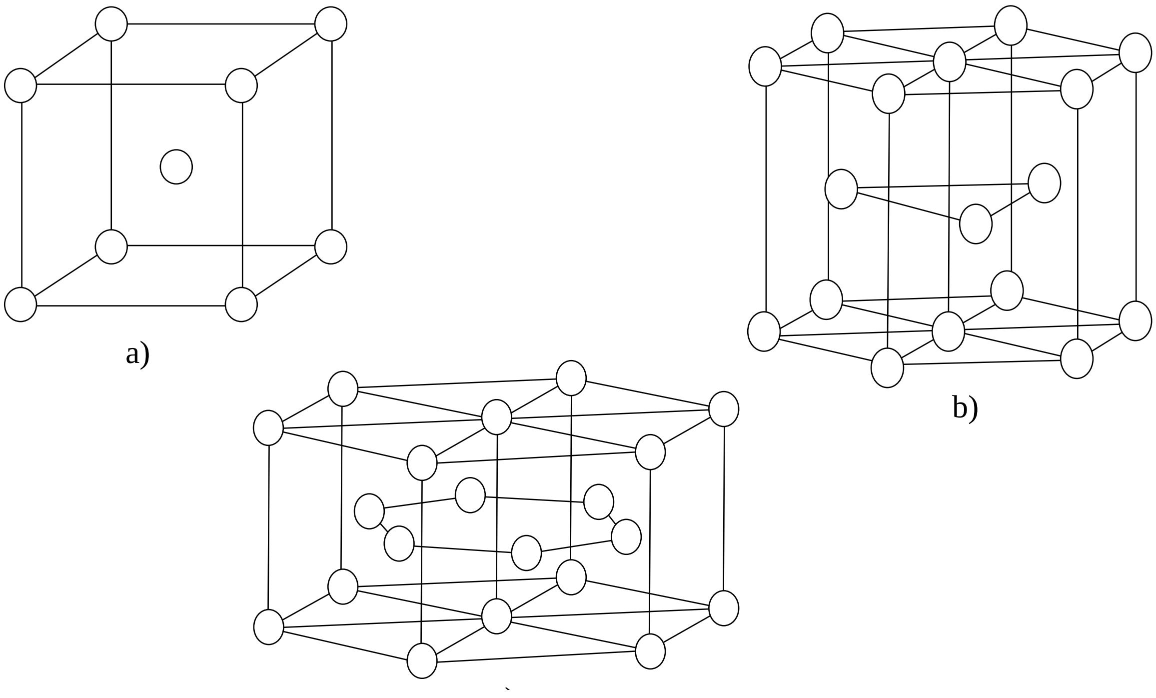

Figure 1. 4 The unit cell of a) α-phase, b) β-phase, and c) ω-phase for pure Ti.

Table 1. 2 Lattice parameters for Ti allotropic phases

Phase	a (pm)	c (pm)	c/a	APF
β	332	-	-	0.68
ω	460	282	0.613	0.68
α	295	466	1.588	0.74

1.2.2 Alloying Elements and Phase Diagrams

Alloying elements of titanium are usually classified by their ability to stabilize either the α or β phase. A few neutral elements stabilize neither of the two phases. Alloying elements of titanium are roughly classified into four main groups according to the type of phase diagram formed which are schematically illustrated in Figure 1.5 (Takashi Maeda, 1988; Welsch, Boyer and Collings, 1993; Donachie, 2000). They are described as follows.

a) Neutral elements: These alloying elements form the continuous solid solutions of α or β phase. Zr and Hf also exhibit this form of phase diagram

b) α stabilizing elements: They form wide α-phase regions with an increasing β-transus temperature. Examples are carbon (C), nitrogen (N), oxygen (O), aluminum (Al), and gallium (Ga).

c) β-isomorphous elements: These are β-stabilizing elements that form a restricted α phase and a stable α + β regions at room temperature. Examples are vanadium (V), niobium (Nb), molybdenum (Mo), and technetium (Tc).

d) β-eutectoid elements: These types of β-stabilizing elements, form a limited range of β-phase, and decompose the β-phase into α-phase plus a compound at low temperatures. Examples are hydrogen (H), beryllium (Be), silicon (Si), chromium (Cr), manganese (Mn), and iron (Fe).

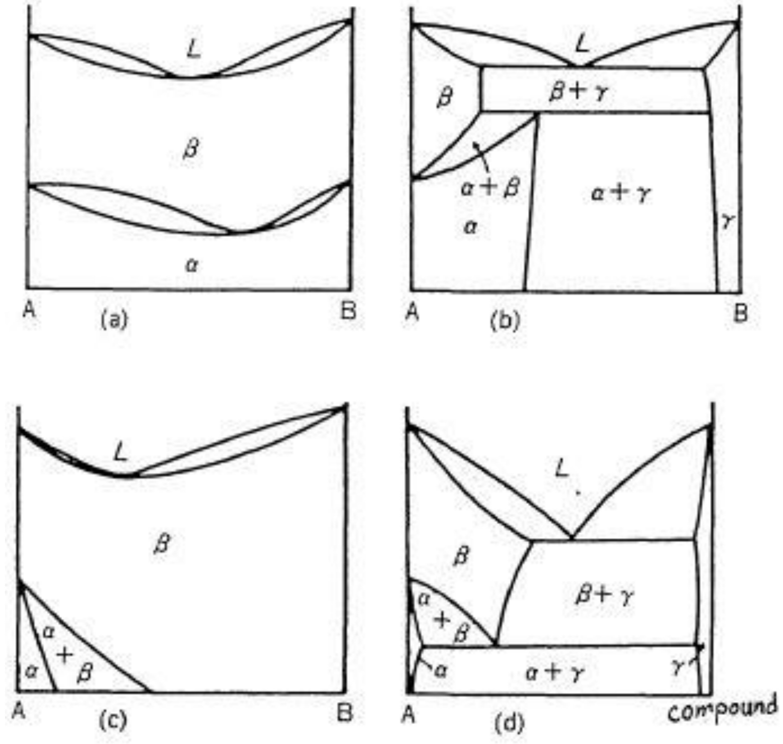

Figure 1. 5 Schematic binary phase diagrams of a) neutral elements, b) α stabilizing elements, c) β-eutectoid elements, and d) β-eutectoid elements with titanium (A=Ti and B=alloying element) (Takashi Maeda, 1988)

A schematic three-dimensional (3D) phase diagram in Figure 1.6 shows the influence of the α-phase stabilizers and the β-phase stabilizers on the phases constitutions (Leyens and Peters, 2003b). Adding a small quantity of β-phase stabilizers (about 1 to 2 wt.%) to the α-phase alloys, results in the formation of near α microstructures, which contain primary α phase and a small fraction of retained β phase (Joshi, 2006). The two-phase mixture, α+β Ti-alloys, usually contain 4-6 wt.% β-phase stabilizers (Joshi, 2006). Further increasing the β-phase stabilizers to about

10-15 wt.% results in metastable/near-β alloys, and in single-phase β alloys for β-phase stabilizers over 20 wt.% (Joshi, 2006).

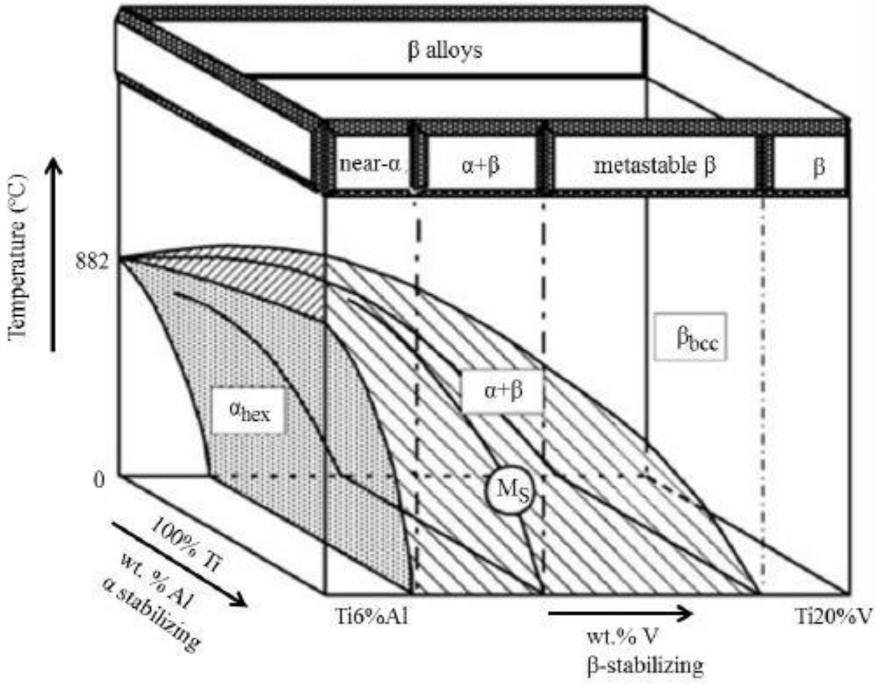

Figure 1. 6 Schematic 3D phase diagram showing influence of the α and β phase stabilizers on Ti. Ms refers to the start of martensitic phase transformation (Leyens and Peters, 2006).

1.2.3 Ti-Al Phase Diagram

Al is an α-phase stabilizer and is widely used alloying element in Ti alloys. The addition of Al raises the β-transus temperature and helps strengthen the α-phase by substitutional solid-solution strengthening. To prevent the precipitation of the Ti_3Al intermetallic phase at RT, the Al content in Ti alloys is usually restricted to 7 wt.% (Joshi, 2006). Figure 1.7 shows the Ti-Al binary phase diagram (Massalski, 1990).

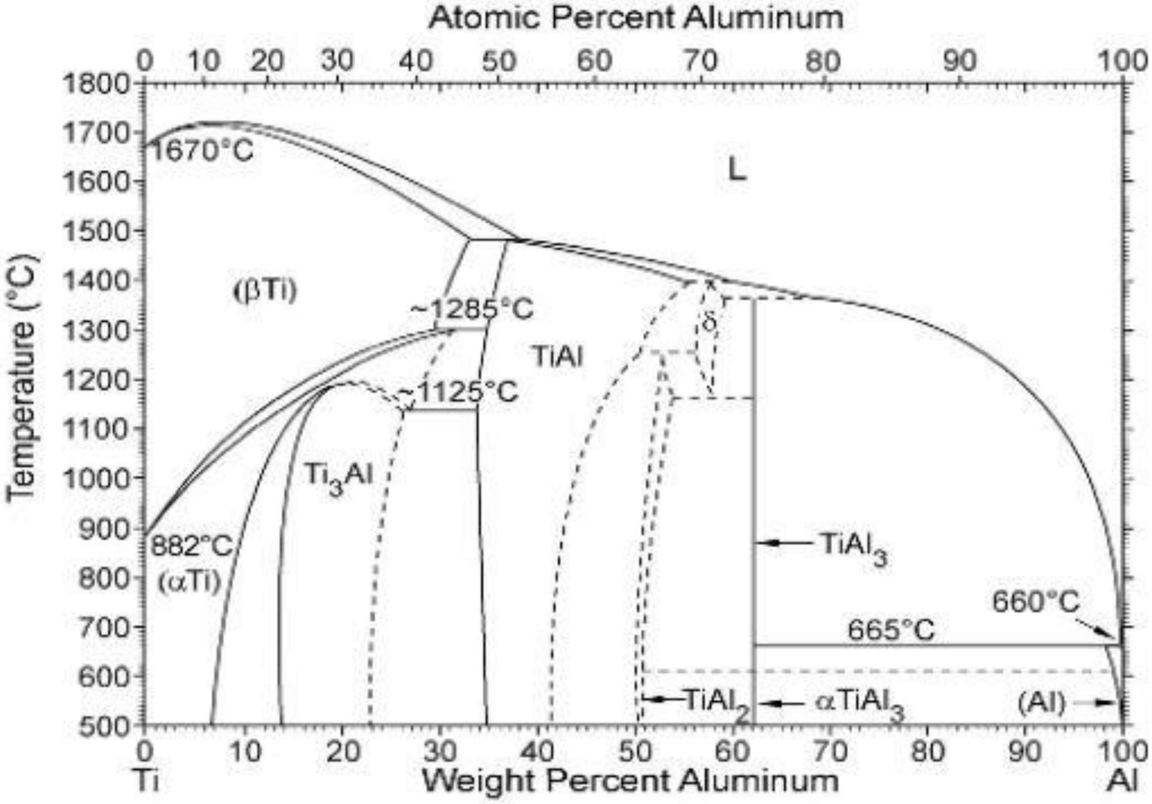

Figure 1. 7 Ti-Al phase diagram (Massalski, 1990).

The addition of Al results in an increase of the *c/a* ratio and leads to a more closed packed basal plane. Due to the smaller atomic radius of Al, 0.125 nm, compared to the atomic radius of Ti, 0.176 nm, a compression of the HCP unit cell is observed when Ti is substituted with Al atoms (Clementi, Raimondi and Reinhardt, 1963).

1.2.4 Ti-Cr phase diagram

Cr is an effective β stabilizing element among the β eutectoid forming elements. The eutectoid temperature being 940 K and the eutectoid point lying at about 15% Cr (Lütjering, G., and Williams, 2003).

The eutectoid decomposition is very sluggish and the precipitation of the intermetallic compound $TiCr_2$ is avoided in Ti alloys with Cr contents below 5% (wt.%). B120VCA alloy with 11% (wt.%) Cr was used in the SR-71 airplane but is unstable because it forms $TiCr_2$ precipitates after prolonged exposure to elevated temperatures (Lütjering, G., and Williams, 2003). The intermetallic ordered structure in the form of the three Laves phases are comprised of three different, but closely-related crystal structures, namely C15 (cubic), C14 (hexagonal), and C36 (dihexagonal) in the Strukturbericht designation (Niinomi, 2008) (Barrett, 1966). The presence of all three Laves phase variants in a single binary system is unusual (Chen, 1996). These phases are stable, and once formed do not easily transform. But these Laves phases do not form immediately upon ageing in the $\alpha+TiCr_2$ phase field. They require prolonged aging and have been observed to have relatively sluggish kinetics (Chen, 1996). P. Samimi et al, proposed the sequence for the formation of $TiCr_2$: $\alpha' \rightarrow \alpha + \beta \rightarrow \alpha + \beta + TiCr_2$ (Samimi *et al.*, 2015). Most β eutectoid forming elements have a low solid solubility in the α-phase. For example, in the Ti-Cr system (see Figure 1.8) the maximum solubility is only about 0.5%.

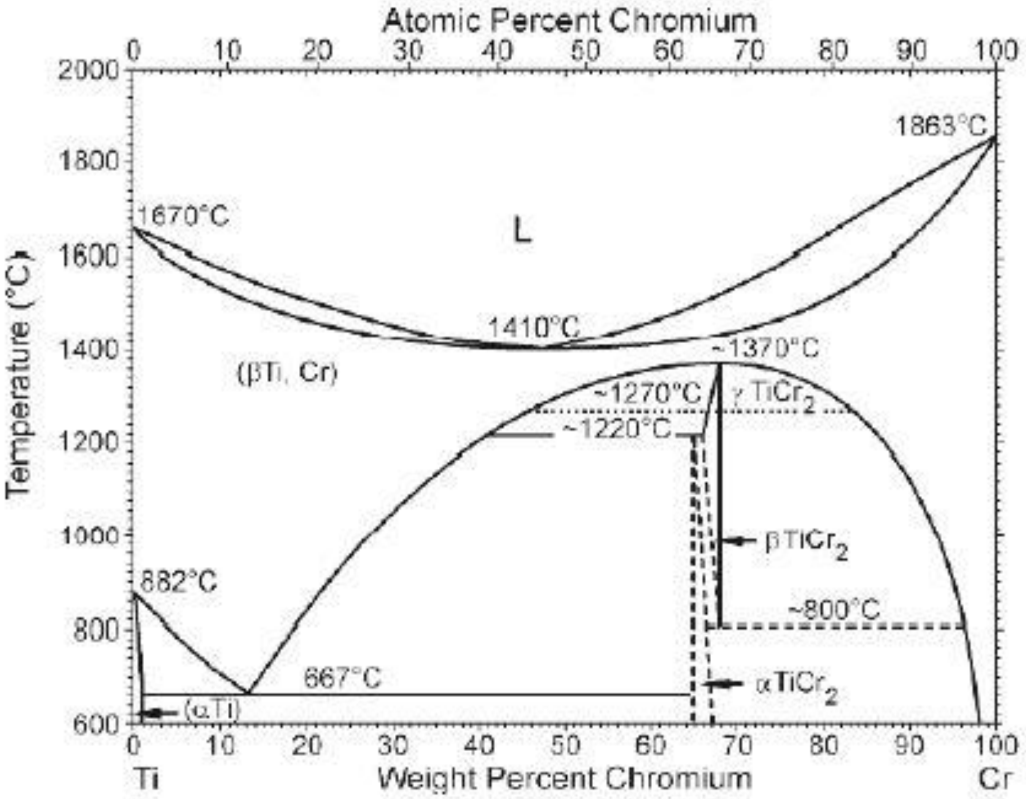

Figure 1. 8 Ti-Cr phase diagram (Baker, 1992).

1.2.5 Ti-Fe phase diagram

Another commonly used β eutectoid forming element is Fe. Fe is a stronger β stabilizer than chromium, and the eutectoid temperature in the Ti-Fe system is about 873 K (Lütjering, G., and Williams, 2003). The formation of the equilibrium intermetallic compound is avoided in Ti-alloys by restricting the Fe content to a maximum of 5.5% (wt.%). This was verified in the recently developed TIMET alloy "low cost beta" (LCB), Ti-1.5Al-5.5Fe-6.8Mo (wt.%) (G Lütjering and Williams, 2003).

The Fe stabilized β-phase also has a higher solubility for hydrogen (H), and thus its presence improves the hydrogen tolerance of this class of titanium alloys. This becomes important since many applications for β-Ti alloys are in corrosive environments where there is a relatively high possibility for pickup of H during service (Leyens and Peters, 2006).

1.2.6 The effect of substitution alloying elements and precipitation on the strength of Ti-alloys

The strengthening mechanisms for Ti-alloys can be classified into: solid solution strengthening, dislocation density hardening, boundary strengthening, precipitate hardening, grain refinement (Lütjering, G., and Williams, 2003). The substitutional alloying elements influence the strength of the Ti-alloys as the alloying elements affect the precipitation of secondary phases (Lee, Ju and Lin, 2002; Li et al., 2002). Lee et al. investigated the effect of Nb content on the mechanical properties of Ti-xNb alloys, where x was between 5 to 35 wt.% (Lee, Ju and Lin, 2002). The amount of Nb affected the crystal structure and morphology of Ti-xNb alloys. For Nb contents less than 15 wt.%, the alloy microstructure was dominated by the hexagonal phase. For Nb contents between 17.5 to 25 wt.%, the alloy microstructure was dominated by the orthorhombic phase. And, for Nb content was higher than 25 wt.%, the alloy microstructure was dominated by the β phase. It was observed that highest strengths were achieved in Ti-10Nb and Ti-27.5Nb, where the dominant phases were orthorhombic and β, respectively.

According to Lütjering and Williams the most effective way to strengthen β-Ti alloys is by precipitation hardening (Lütjering, G., and Williams, 2003). Thermal and/or mechanical processing and alloying content have a strong influence on the morphology, volume fraction, size, and distribution of the ω and α precipitates formed in β-Ti alloys (Ankem and Greene, 2002; Nag *et al.*, 2009a). Precipitates obstruct the movement of dislocations and add strength and toughness. A significant amount of research has been done on near β and β-Ti alloys correlating the mechanical properties with the microstructural changes. For example, in Ti-13Mo-7Zr-3Fe (wt.%) alloy, an increase in the hardness value was observed after aging due to a refined scale of the α-phase as shown in Figure 1.9 (Banerjee et al., 2004).

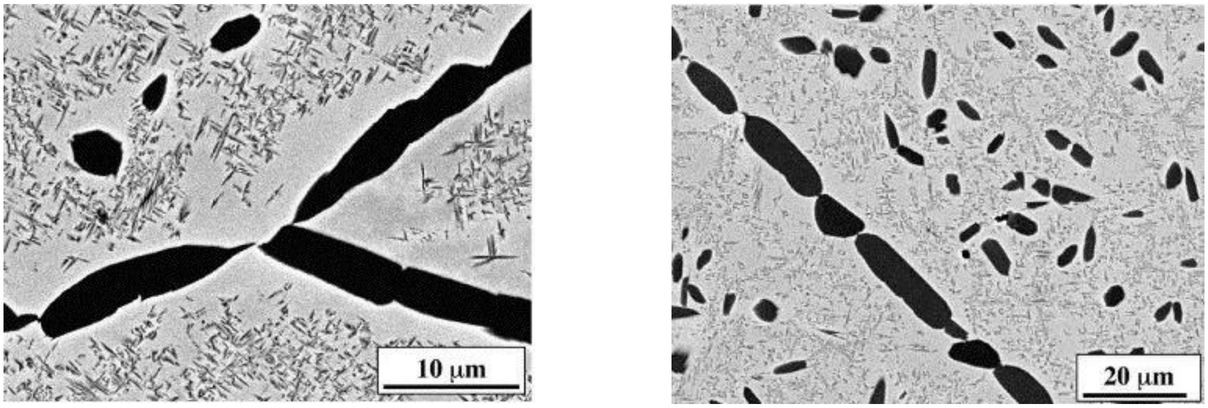

Figure 1. 9 BSE SEM photomicrographs of aged Ti-12Mo-6Zr-2F sample which exhibited fine secondary α-phase particles.

According to Dubinskiy et al. ω-phase precipitates in Ti-alloys are classified into three types based on their transformation behavior (Kuan, Ahrens and Sass, 1975; Lütjering, G., and Williams, 2003; Dubinskiy *et al.*, 2016):

- Athermal ω (ωath) – martensitic transformation caused during quenching
- Isothermal ω (ωiso) – diffusion-controlled process during aging
- ω – Induced by deformation process

Lütjering and Williams also found that ω_{iso} has an ellipsoidal or a cuboidal shape (Lütjering, G., and Williams, 2003). Hickman found that the ω-phase can form during quenching, during aging at temperatures between 373 K and 773 K, or during mechanical deformation (Hickman, 1969). In Ti-20V, the ω-phase formed at lower temperatures and longer aging times as shown in Figure 1.10. Hickman also found that the ω-phase results in an increase in both the strength and hardness, while decreasing the elongation-to-failure (ε_f) (Hickman, 1969).

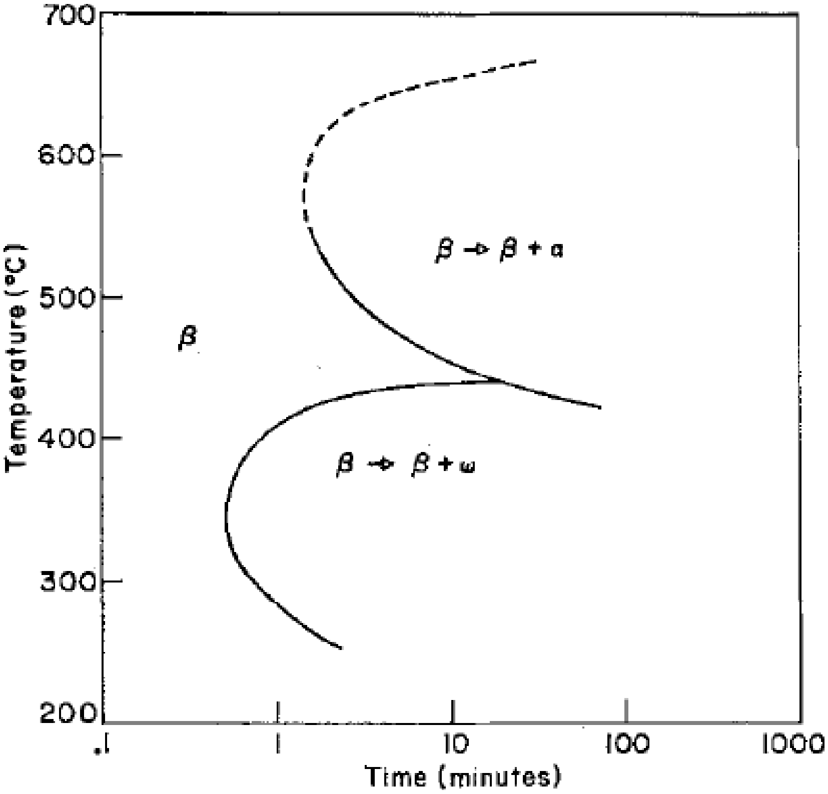

Figure 1. 10 Schematic temperature vs time plot for Ti-20V. The ω-phase forms at lower temperatures and for longer aging times (Hickman, 1969).

1.2.7 The effect of heat treatment on the strength of Ti-alloys

Thermal treatment of Ti-alloys significantly contributes to its strength due to precipitation formation by diffusion (Lütjering, G., and Williams, 2003). The creation of precipitates, their size, geometry, and volume fraction can be controlled by aging treatments which in turn affect the strength of the Ti-alloys (Donachie, 2000; Dehghan-Manshadi and Dippenaar, 2011; Chen et al., 2014). The most common method for thermal treatment for metastable β-Ti alloys is solution treatment above the β transus temperature followed by an aging step.

The thermal effects on the strength of Ti-35Nb-7Zr-5Ta-xO (wt. %) was studied by Qazi et al. by solutionizing above the β transus temperature followed by an aging step (Qazi et al., 2005). For 0.06 O wt.%, ω-phase formation was observed at 700 K and this provided strengthening. The maximum strength was observed in a 0.46 wt.% O alloy after a 755 K heat treatment due to both α and ω-phase precipitation (Qazi et al., 2005). Similar strengthening has been observed in other β-Ti alloys during aging between 623 K and 873 K for about 12 days (Qazi *et al.*, 2005).

1.3 Creep Testing and creep mechanisms

1.3.1 Creep testing

Creep is a time dependent deformation process in materials under a constant load below the yield stress particularly at elevated temperatures. At ambient temperature, with most materials, this deformation is so slow that it is not significant. At higher temperature, the rate of deformation increases at an applied load and it becomes vitally important to know the speed of deformation at a given load and temperature if components are to be safely designed for high temperature service. Failure to be able to do this may result in, for example, the premature failure of a pressure vessel or the fouling of gas turbine blades on the turbine casing.

Creep tests are usually conducted using a tensile specimen to which a constant stress is applied, often by the simple method of suspending weights from it. Surrounding the specimen is a thermostatically controlled furnace and the temperature is measured by a thermocouple attached to the gauge length of the specimen as shown in Figure 1.11. The extension of the specimen is measured by a very sensitive extensometer as the actual amount of deformation may be between two to three per cent.

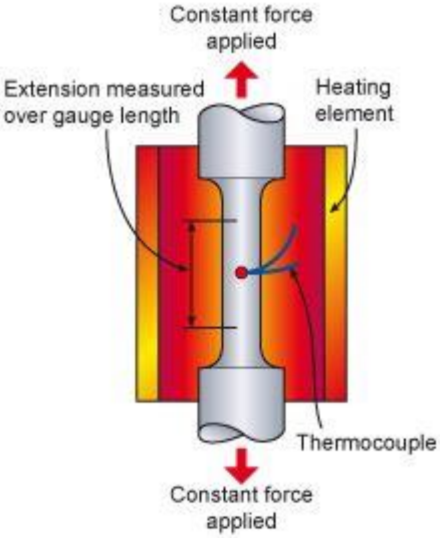

Figure 1. 11 Schematic diagram of a creep test (https://www.twi-global.com/technical-knowledge/job-knowledge/creep-and-creep-testing-081)

The results of the test are then plotted on a graph of strain versus time (see Figure 1.12). Testing is generally carried out in air at atmospheric pressure. However, if the material is to operate in an aggressive environment then the testing may need to be carried out in a controlled environment simulating service conditions.

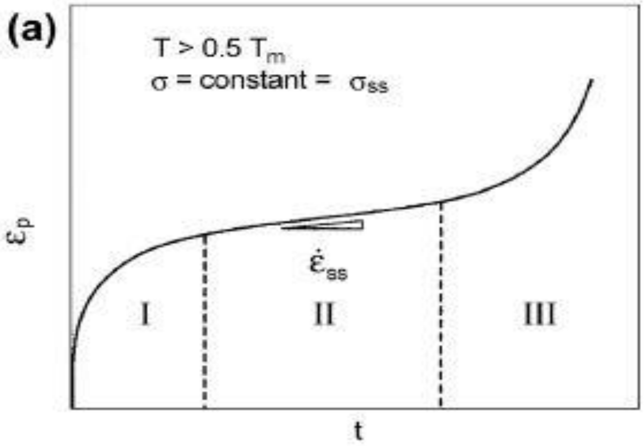

Figure 1. 12 Typical creep strain vs time plot for pure metals (Kassner, 2015)

The three stages of creep shown in Figure 1.12 are:

- Primary Creep: The creep rate decreases with time.
- Secondary Creep: It is also called steady state where the creep rate is constant with respect to time.
- Tertiary Creep: The creep rate increases with time.

The creep behavior of Ti-3Al-2.5V (wt.%) was evaluated by Gollapudi et al., under a wide range of stresses and temperatures, and the deformation modes were characterized as a function of the testing parameters (i.e. stress and temperature) (Gollapudi, Charit and Murty K, 2008). The effect of alloying element content on the creep deformation behavior of Ti-6Al-2Sn-4Zr-2Mo (wt.%) was studied by Hayes et al. (Hayes R, Vishwanathan G and Mills M, 2002). Jenkins et al. studied the creep properties of duplex-annealed Ti-8Al-1Mo-1V (wt.%) alloy at temperatures of 600 F, 800 F, 1000 F, and 1200 F (D. and A., 1968).

1.3.2 Creep mechanisms

The deformation mechanisms controlling the secondary steady-state creep behavior of pure metals and single-phase alloys are the most thoroughly understood because the secondary steady state strain rate (ε_{aa}) can be measured experimentally and used to suggest the dominant deformation mechanism. There are two broad mechanisms by which steady state creep takes place: diffusion creep and dislocation creep.

- Diffusion creep: This type of creep occurs by transport of material via diffusion of atoms within a grain. It is driven by a gradient of free energy (chemical potential), which in this case, is created by the applied stress. There are two types of diffusion creep mechanisms depending on the diffusion paths.

- Nabarro-Herring Creep: The deformation of a metal due to the stress directed flow of vacancies through the crystal lattice (Nabarro, 1948; Herring, 1950). A standard form of the Nabarro-Herring (N-H) equation for strain rate is given by:

$$\dot{\varepsilon} = \frac{10\sigma D_L \Omega}{d^2 kT} \tag{1.1}$$

Where $\dot{\varepsilon}$ is the strain rate, σ is the applied stress, D_L is the lattice diffusion coefficient, Ω is the vacancy volume, d is the grain size, k is Boltzmann's constant, and T is the absolute temperature (Nabarro, 1948)

- Coble Creep: This model of creep deformation occurs due to vacancy diffusion through the grain boundaries, rather than through the crystal lattice (Coble, 1963). The equation Coble derived for the strain rate occurring from vacancy diffusion through the grain boundaries is given by:

$$\dot{\varepsilon} = \frac{148\sigma DBW\Omega}{d^3 kT} \tag{1.2}$$

where $\dot{\varepsilon}$ is the strain rate, σ is the applied stress, D_B is the grain boundary diffusion coefficient, W is the width of the grain boundary, Ω is the vacancy volume, d is the grain size, k is Boltzmann's constant, and T is the absolute temperature.

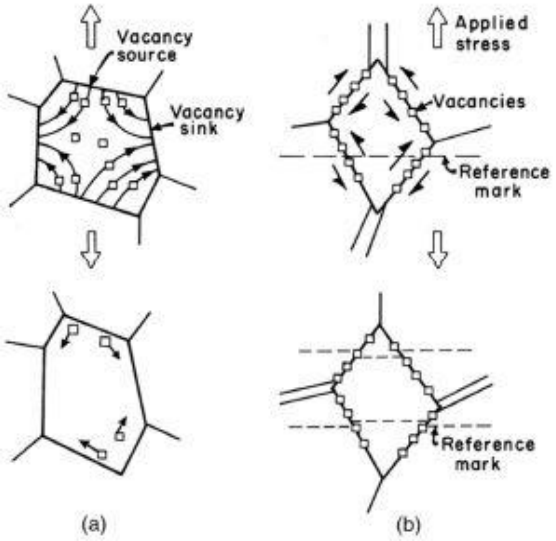

Figure 1. 13 Schematic representation of a) Nabarro-Herring creep and b) Coble creep (Meyers and Chawla, 2008)

- Dislocation creep: This type of creep mechanism involving motion of dislocations. This mechanism of creep tends to dominate at high stresses and relatively low temperatures. Dislocations can move by gliding in a slip plane which requires very little thermal activation. However, the rate-determining step for their motion is often a climb process, which requires diffusion and is thus time-dependent and favored by higher temperatures. Obstacles in the slip plane, such as other dislocations, precipitates or grain boundaries, can lead to such situations (Metallurgy, 1986). and the equation that describes the strain rate dependence is:

$$\dot{\varepsilon} = B\sigma^{n} \exp\left(\frac{-Qapp}{RT}\right) \tag{1.3}$$

where $\dot{\varepsilon}$ is the strain rate, B is a constant, σ is the applied stress, n is the creep stress exponent, Q_{app} is the activation energy for creep (in kJ/mol), R is the gas constant, and T is the absolute temperature

Dislocation viscous glide mechanism, with a n value of about 3, is a process in which the dislocations movement is impeded due to their interaction with the solute atoms in several possible ways (Sherby, Anderson and Dorn, 1951).

- Grain Boundary Sliding: At elevated temperatures, the grains in a polycrystalline metal can move relative to one another which is referred to as grain boundary sliding (GBS) (Metallurgy, 1986). GBS process, typically, is considered to accommodates deformation due to a diffusional or dislocation controlled deformation mechanism (Metallurgy, 1986).

The values of creep stress exponents give insight into the deformation mechanisms that might occur during the secondary stage of creep. These parameters are typically calculated using Equation 1.3 after the minimum creep rate is determined directly from strain versus time data collected from actual creep experiments. Table 1.1 provides the creep exponent values for the different creep mechanisms.

Table 1. 3 List of creep mechanisms and their corresponding creep exponent values

Creep mechanism	Creep exponent value ‘n’
Nabarro-Herring	1
Coble	1
GBS	2
Dislocation climb	~5
Dislocation viscous glide	~3

1.4 Work performed

In this thesis work, the creep properties of three different β-Ti alloys, Ti-12Cr-1Fe-3Al (wt. %) (TCFA), Ti-12Cr-3Al (wt. %) (TCA), T-12Cr (wt. %) (TC), were measured and compared. The microstructures for these alloys were studied before and after creep using various characterization techniques. The material was supplied by Professor Masahiko Ikeda of Kansai University, Kansai, Japan.

In Chapter 1, a brief overview of Ti and Ti-alloys is provided, including their crystal structure and commonly used alloying elements. The influence of alloying, precipitation, and heat-treatment on the strength of bcc Ti alloys are discussed. A background on creep and its mechanisms is provided.

In Chapter 2, the experimental procedures used in this thesis work are described. Bulk alloy compositions are provided in this chapter. In addition, this chapter covers details of the experimental set-up for the creep experiments and volume percentage of the precipitate phase(s).

In Chapter 3, the results from the microstructure characterization and the creep experiments are presented. The grain sizes for the β-phase in the alloys were measured using the line-intercept method from back scattered electron images (BSE) (‘Test Methods for Determining Average Grain Size’, 2010). Volume percentage of the precipitate phase(s) were measured using ImageJ software from BSE photomicrographs. X-ray diffraction (XRD) was performed on the as-processed alloys, heat-treated samples, and creep tested samples to investigate the phases present. Creep tests were conducted on the material at stresses ranging from 200 MPa-350 MPa at 683 K. The surface microstructure after each test was captured by SEM images. Results for the creep strain vs time analysis for the alloys was for every test were presented. The microstructure of the three alloys and how they affect the creep trends obtained is discussed.

In Chapter 4, the conclusions of this thesis work are presented, and potential future work is suggested.

CHAPTER 2

EXPERIMENTAL PROCEDURES

2.1 Material

Three β-Ti alloys were studied in this work. All the studied alloys were levitation melted in a 2-kg, 90Dx80L LEV levitation induction furnace. They were then hot forged into blocks of dimension 25 x 60 x 250 -mm^3 at approximately 1320 K. The alloys were then subjected to homogenization annealing at 1173 K for 1 hour in vacuum. The quenching process was carried out at 34.7 K/s (Cooling rate) in ice water (J Ballor *et al.*, 2019). Figure 2.1 shows the as-processed alloys, which were processed by Daido Steel Corporation (Nagoya, Japan). Maintaining a high cooling rate helps obtain a uniform β microstructure without the presence of the α-phase (Ikeda *et al.*, 2004). Table 2.1 provides the measured Cr, Al, Fe contents of each alloy, measured using inductively coupled plasma atomic emission spectroscopy (ICP-AES). Using nondispersive infrared spectroscopy (NDIR), the O, C, and N contents were determined by the Daido Steel Corporation (Nagoya, Japan).

Table 2. 1 Measured compositions of the alloys studied**

Alloy		Chemical composition						
		Ti	Cr	Fe	Al	C	O	N
Ti-12Cr (TC)	wt.%	Bal.	12.1	0.02	0.01	0.004	0.059	0.004
	at.%	Bal.	11.2	0.02	0.02	0.02	0.18	0.01
Ti-12Cr-3Al (TCA)	wt.%	Bal.	12.3	0.02	3.06	0.003	0.062	0.004
	at.%	Bal.	11.2	0.02	5.35	0.01	0.18	0.01
Ti-12Cr-1Fe-3Al (TCFA)	wt.%	Bal.	12.4	0.93	3.02	0.003	0.11	0.004
	at.%	Bal.	11.3	0.79	5.28	0.01	0.32	0.01

**Table taken from Ballor et al. 2019

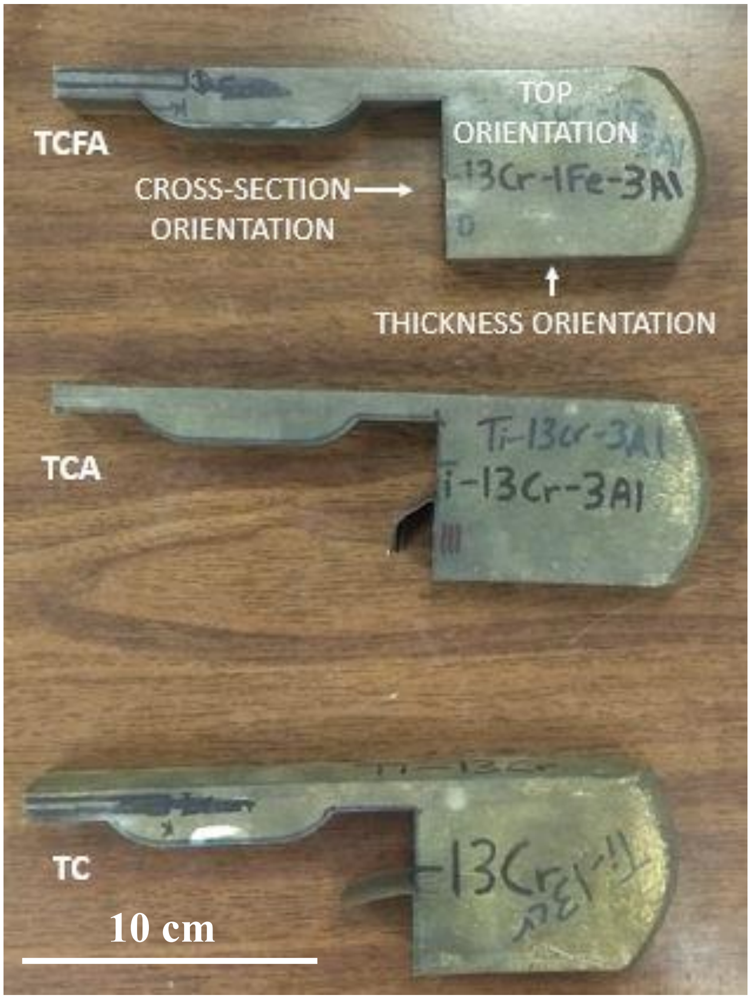

Figure 2. 1 An image showing the three as-processed alloys with EDM cuts from where the samples for the creep tests were extracted. The top, cross-section and thickness orientations are shown.

2.2 Microstructural Characterization

2.2.1 Metallographic sample preparation

The creep samples were machined using electric discharge machining (EDM). All the samples were mechanically polished prior to creep testing. First, the samples were ground and polished using silicon carbide (SiC) papers progressively from 120 to 2400 grits. About 5 to 10 minutes were spent at each polishing step until the scratches from the previous SiC paper was removed. Water was used to rinse the specimens before moving to the next grinding step. Next, 3 µm, 1 µm, 0.5 µm, and 0.25 µm diamond pastes were used to obtain a mirror finish. Each polishing step was around 15 minutes with water rinsing in between steps. The final polishing step used a solution consisting of a 5:1 ratio of Struers OP-S Colloidal silica (0.02–0.04 micron) and 30% hydrogen peroxide. This step required around 30 minutes of polishing time. The polishing cloth used in this step was purchased from Buehler (catalog No. M500-12PS). After polishing, water was used to rinse away the colloidal silica. The samples were ultrasonically cleaned in ethanol to remove the residual colloidal silica.

The samples were also etched for about two minutes using Kroll's reagent (commonly used chemical etchant for titanium) before observing under the microscope. The etchant consisted of 100 ml water, 1-3 ml hydrofluoric acid and 2-6 ml nitric acid.

2.2.2 Scanning Electron Microscopy

The microstructure of the alloys investigated was characterized using scanning electron microscopy (SEM). The SEM used in this work was a field emission gun Tescan Mira 3 SEM (Figure 2.2). Both secondary electron (SE) and back-scattered electron (BSE) images were acquired before and after the creep experiments.

Grain sizes were determined using BSE photomicrographs. The different phases could be distinguished using BSE imaging. Phases containing larger average atomic numbers appear brighter in BSE images than phases containing lower average atomic numbers (Flegler S.L., Heckman J.W.Jr., 1993). The possible α-phase and ω-phase of the Ti alloys evaluated in this study appeared dark or grey due to its low average atomic number (Al is the most common α-phase stabilizer and it has an atomic number of 13, and the ω-phase is considered to be Ti rich which has an atomic number of 22) while the β-phase appeared brighter because it is enriched V (V is the most common β stabilizer and it has an atomic number of 23) (Boyer, Welsch and Collings, 1994) . The average β-phase grain size was measured from the SEM images according to ASTM standard E112-12 (ASTM International) ('Test Methods for Determining Average Grain Size', 2010).

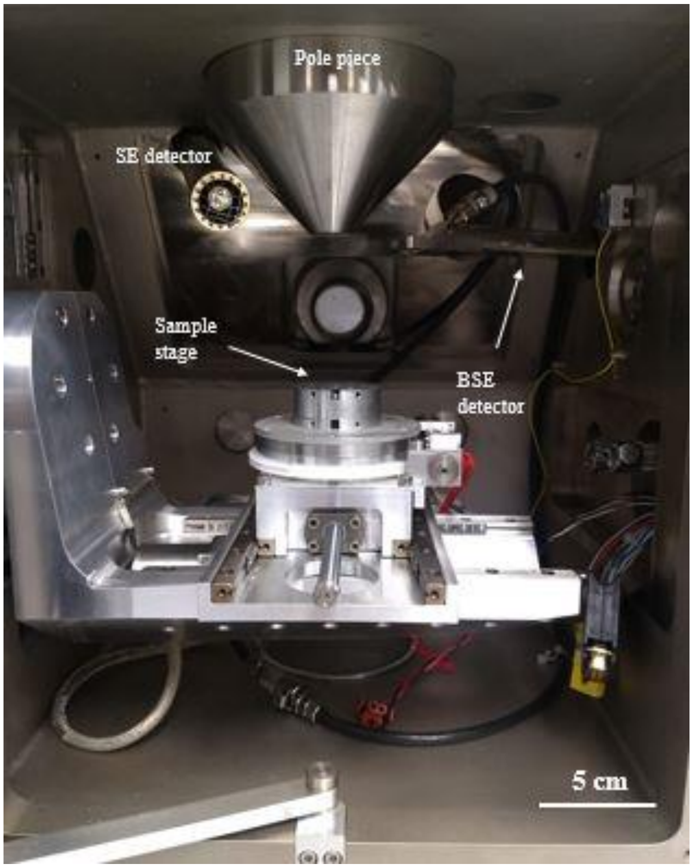

Figure 2. 2 A photograph showing Tescan Mira3 SEM chamber

2.2.3 Sample preparation and measurement of precipitate volume fraction

The BSE photomicrographs used to calculate the volume fraction of precipitates were captured using the Regulus 8200 ultra-high-resolution SEM at Hitachi High Tech Americas, Maryland.

The samples were first mounted on a stub using hot glue. Then the samples were mechanically polished using SiC paper of 180 grit and 1200 grit on the cross-sectional face. Next, cross-sectional milling was performed using an ion milling system, IM4000 Plus, at an accelerating voltage of 6 kV and a milling period of 2 hrs. The samples were analyzed for topographical information using the Regulus SEM, operating at a voltage of 5 kV.

The volume fraction of the precipitate phase(s) was calculated using ImageJ software. ‘Threshold’ function was used and adjusted to color the phase of interest. The function allowed the determination of the area fraction of a particular phase in the BSE image. This area fraction translated to the volume fraction of the phase (Hariharan, 2018). A similar technique was applied to multiple BSE images and the volume fractions were averaged.

2.2.4 X-ray diffraction analysis

X-Ray diffraction (XRD) was performed on the alloys with a Bruker - D2 PHASER diffractometer (see Figure 2.3) in the Bragg–Brentano orientation using Cu-Kα radiation with a characteristic wavelength of 1.54 Å and a Ni filter. Each sample scan used a step size of 0.02°/step, a count time of 1 second, and a 2θ range of 20° - 90°. All scans were conducted with a tube current of 35 mA and a tube voltage of 35 kV. First, the sample holder was scanned, and the spectrum was recorded. Scans were analyzed using Bruker’s EVA software tool. Background intensities were found from EVA software (EVA uses DIFFRAC method to calculate the background). Then background intensities were then subtracted from the raw intensity data and Kα2 stripping was performed (EVA software). The final sample spectrum was obtained by subtracting the sample holder spectrum from the sample spectrum.

Figure 2. 3 A schematic showing the geometry of the test specimens used in the creep experiments. The dimensions are in millimeters

The 2θ peak locations were also found by EVA software (uses a mechanism called peak force tapping) for the scans. The d-spacings were calculated using the calculated 2θ values and Bragg's law, shown in Equation 2.1 below, where λ is the radiation wavelength in Å, θ is the calculated 2θ angle divided by 2, and d is the d-spacing in Å. By rearranging Bragg's law, d can be solved for directly, shown in Equation 2.2. 1.54Å was used as λ for Cu-Kα radiation in all calculations (Cullity and Stock, 2001).

$$\lambda = 2 * d * \sin(\theta) \tag{2.1}$$

$$d = \frac{\lambda}{2*\sin(\theta)} \tag{2.2}$$

For phase analysis, peak locations for the α, ω, and $TiCr_2$ phases were found in the literature (Sugano and Ikeda, 2005; Ogawa *et al.*, 2007, 2008; Kolli, Joost and Ankem, 2015). 2θ locations were found by taking the figures from the literature and placing them into an online digitizer with a magnified pointer. The error involved in this method was ±1.63° due to the size of the pixels. The markers for the different peaks also did not have a clear "center" which contributed to the error. Because of this, the phase analysis is highly qualitative and must be re-evaluated using EBSD technique. Intensity ratios could not be obtained from these figures. The list of all the theoretical peaks can be found in Table 2.2.

To improve the qualitative analysis three filtering steps were used. 1) Peaks with no evidence in the literature were removed. 2) Peaks with unconvincing evidence were removed i.e. any data point that was less than or equal to the 4% over the background intensity was set to zero. 3) Any peak convoluted with β peak was removed (as there was no method available to deconvolute them). After the above filtration, minor peaks in the data were more visible. Matching the theoretical peaks to the data was done by looking for small "bumps" in the data or relatively dense clusters of peaks. Phases were identified by overlaying the final processed intensity data with lines showing all possible peak locations from literature.

Table 2. 2 A list of all the theoretical peaks locations for the α, ω, and $TiCr_2$ phases from literature

α (º 2θ)	ω (º 2θ)	$TiCr_2$ (º 2θ)
35	51	37
38	65	43
40	79	45
41	80	
53		
63		
70		
71		
74		
76		
77		
78		
82		
87		

2.3 Creep Testing

2.3.1 Sample configuration

For the creep mechanical testing, flat dog-bone specimens with dimensions of about 7 ± 0.2 mm gage width, 1.1 mm ± 0.2 mm thickness, and 122 mm length were EDM cut. Figure 2.4 shows a photograph of an EDM cut specimen. The samples were polished using the method described in section 2.2.1

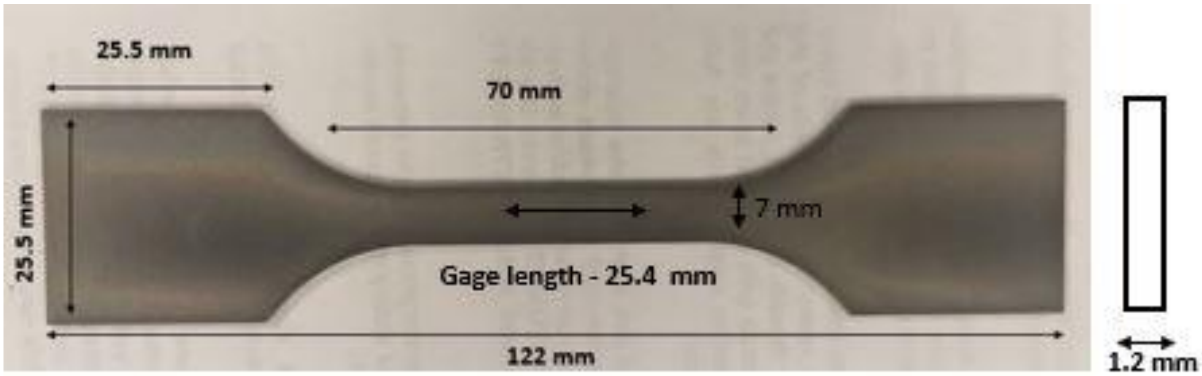

Figure 2. 4 A photo of a sample representative of those used in the creep experiments. The sample dimensions are provided.

2.3.2 Creep test experiment

Conventional uniaxial constant load constant temperature creep tests were performed using Applied Test Systems (ATS) (Butler, PA) 2400 series creep frames (see Figure 2.5). The creep frame was equipped with a high temperature split tube furnace with a maximum temperature of 2073 K, and a contact type extensometer attached to a linear variable differential transformer (LVDT) to measure the strain. The creep tests were conducted in an open-air environment. A gage length of 1 inch (25.4 mm) was used as standard for deflection measurement. The creep testing conditions of the three alloys are listed in Table 3.1.

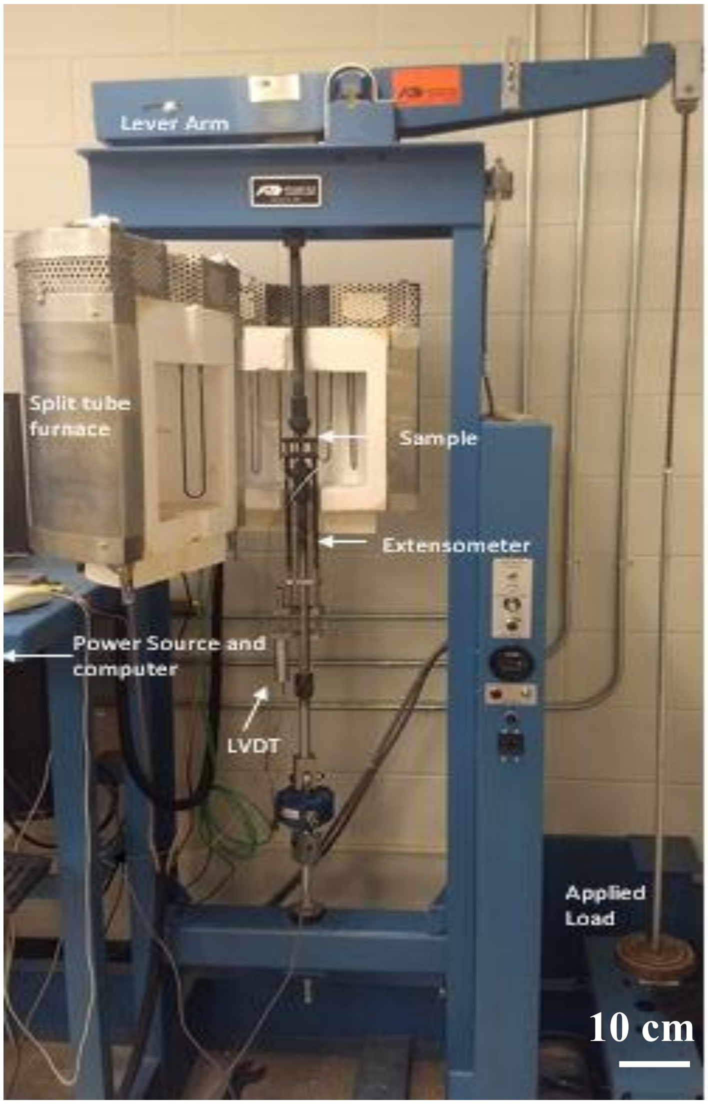

Figure 2. 5 Photograph showing the creep frame and the sample setup representative of all the creep experiments.

The temperature range for the phase transformations from β-phase to α and/or ω phase(s) in a Ti-12Cr-1Fe-3Al (wt. %) (TCFA) alloy was found to be 653 K to 723 K (Khademi, 2018). For this study, the creep tests were conducted at, 200 MPa, 250 MPa, 300 MPa, and 350 MPa, and at 683 K.

Prior to creep testing, all the samples were heat treated for 48 hrs inside the creep frame furnace (i.e. in an open-air environment) at the creep temperature under no load. The approximate duration of the tests was about 336 hours (14 days), and all the tests were stopped in the secondary creep regime. None of the samples were taken to failure.

2.4 Heat treatment

To understand the thermal effects on the phases in the alloys, a separate set of samples were subjected to only heat treatment followed by analyzing with the Bruker X-Ray Diffractometer. Small rectangular samples of dimension of about 15 mm x 15 mm were cut from the grips of the dog-bone samples using a low speed cutting blade. All the rectangular samples were polished up to 1200 grit (emery paper) to reduce any background noise from surface roughness. These samples were placed in a cylindrical quartz tube which was first evacuated to ensure a low-pressure environment. For real-time temperature measurement, a test set up was designed and fabricated as shown in Figure 2.6. The samples were heat treated at four different temperatures, 683K, 623 K, 573 K, and 483 K, for about 12 hrs. For each scan, the top orientation was placed in the face up position inside the Bruker X-Ray Diffraction chamber.

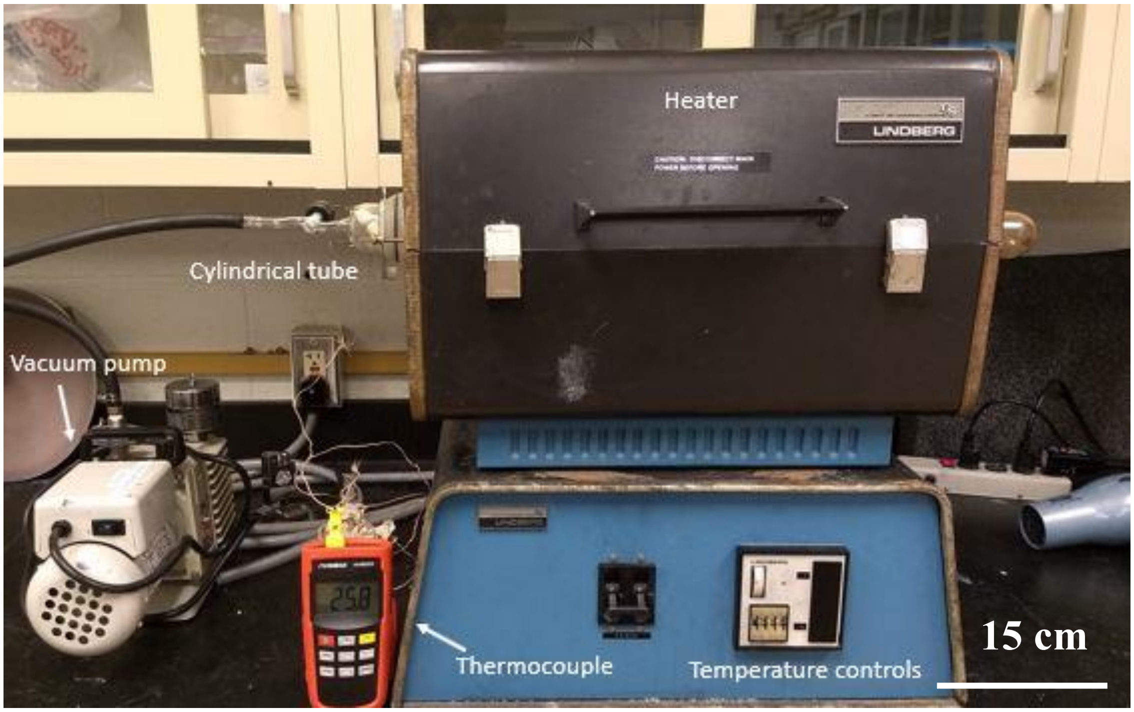

Figure 2. 6 Image of the furnace used for the heat treatments. The real-time sample temperature was measured during the heat treatment.

2.5 Hardness measurements

Vickers microhardness testing was performed on the samples according to ASTM Standards E92-17 (ASTM E92-17, 2017). This testing was performed using a 500 g-force load and a dwell time of 10 s (Figure 2.7). Six readings were made at each of the locations and the hardness values (HV) were reported. The hardness testing was performed on the as-processed samples, the grips of the creep tested samples (subjected to heat treatment and minimal creep deformation), and the gage sections of the creep-tested samples (subjected to both heat treatment and creep deformation).

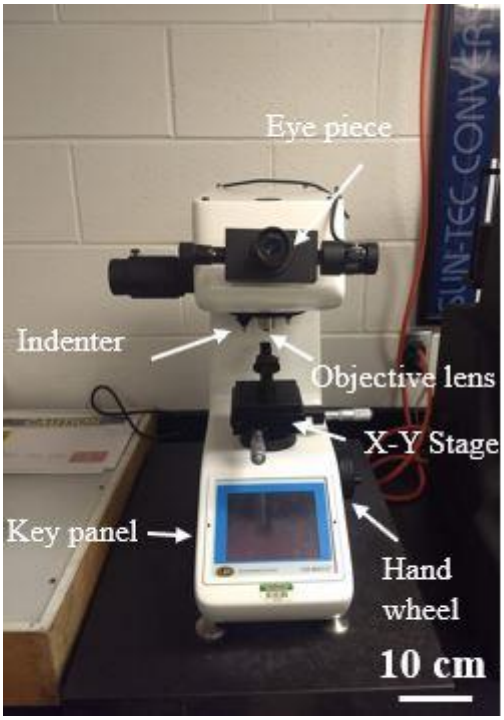

Figure 2. 7 Image of the Vickers hardness testing machine.

2.6 Creep data analysis

Deformation data as a function of time was collected from the creep frame for all the samples. Kaleidagraph, a data analysis and graphing software, was used to display creep strain vs time plots for all the samples. A power law (see Equation 2.3) was used to calculate the creep exponent values. By substituting the different stresses and their corresponding steady state creep rates for a creep temperature in Equation 2.4, a plot of logarithm steady state creep rate and logarithm stress was obtained and the slope (i.e. creep stress exponent) was calculated.

$$\epsilon_{ss} = B \mid \sigma \mid^{n} e x p \left(- Q / k T\right) \tag{2.3}$$

$$\ln \epsilon_{ss} = \ln B + n \ln \sigma - Q / k T \tag{2.4}$$

A Matlab code was used to calculate the strain rate from the strain values for the alloys (see appendix). Strain rate vs time plots were generated to verify if crept samples were stopped in the secondary creep regime and had a steady state creep rate (discussed in Section 3.3.2).

Deflection data of the samples as a function of time was also collected from the creep frame during the 48 hr heat treatment under no load prior to creep testing. Deflection vs time plots were generated for the samples to determine possible phase transformations occurring during this period.

CHAPTER 3

RESULTS AND DISCUSSION

3.1 Microstructural characterization

3.1.1 XRD results

The XRD results for the as-processed materials revealed peaks corresponding to the β phase (see Figure 3.1)

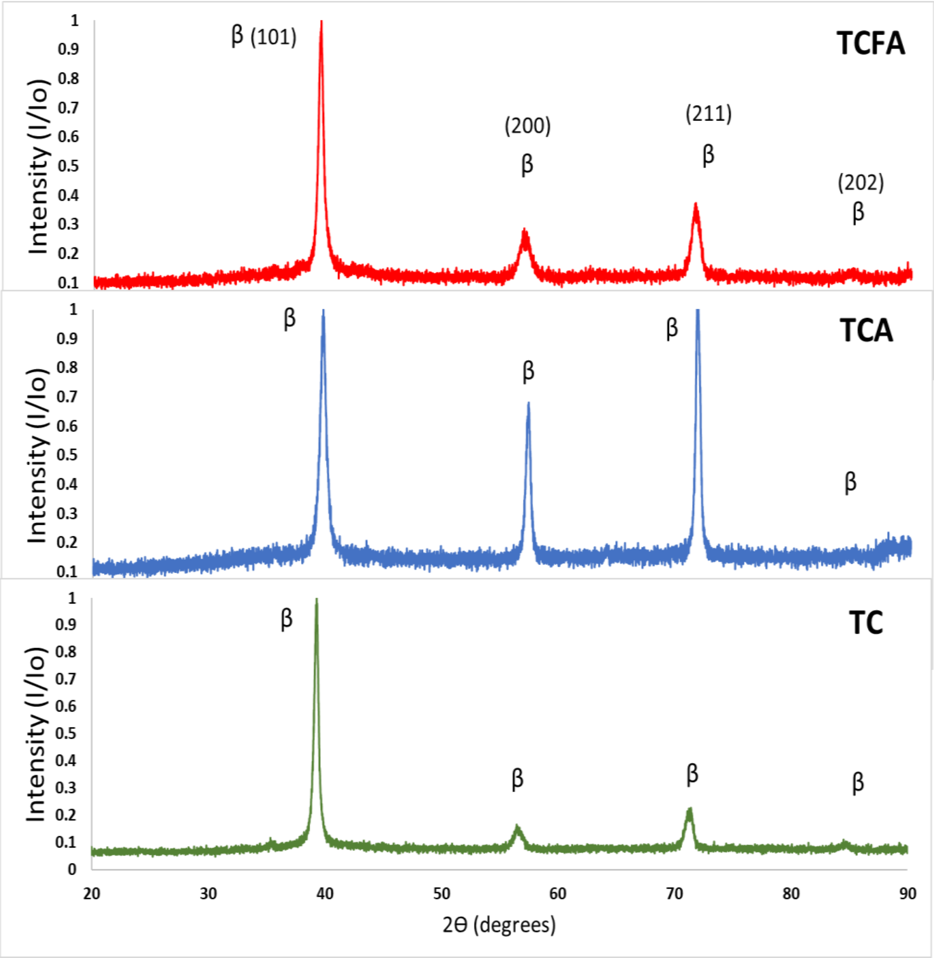

Figure 3. 1 XRD data in the form of Integrated intensity vs 2θ for the studied alloys which exhibited only β phase peaks

From the integrated intensity values, TCA exhibited a (211) β-phase peak which was almost three times greater than that of the other two alloys. The addition of Al may be responsible for the observed texturing. The further addition of Fe to Ti-12Cr-3Al (wt. %) seems to reduce the peak intensity for (211) β-phase peak. The changes in the atomic radii of the individual elements was likely the cause for the slight shift in the β-phase peak positions for the three alloys. The lattice parameters for the β-Ti was calculated for the three different alloys using Bragg's law (refer to Equation 2.1).

$$\lambda = 2 * d * \sin(\theta) \tag{2.1}$$

A decrease of about 0.02 Å was found going from the pure Ti (Theoretical value – ASM Handbook, vol. 9, pp. 899– 917) to TC. Similarly, a decrease of 0.04 Å was found on addition of Al to TC, and a decrease of 0.02 Å on addition of both, Al and Fe to TC. Although the change observed in the lattice parameter was small it may have influenced the hardness and the strength of the alloys.

The XRD patterns of the samples after heat treatment for 12 hrs at 683 K indicates possible ω and α-phase peaks. The peak locations for the α, ω, and $TiCr_2$ phases found in the literature (Ikeda *et al.*, 2004; Gunawarman *et al.*, 2005; Ogawa *et al.*, 2008) for metastable β-Ti alloys was used to identify the peaks as shown in Figure 3.2. To improve the qualitative analysis, peaks below 5% of the background intensity were set to zero.

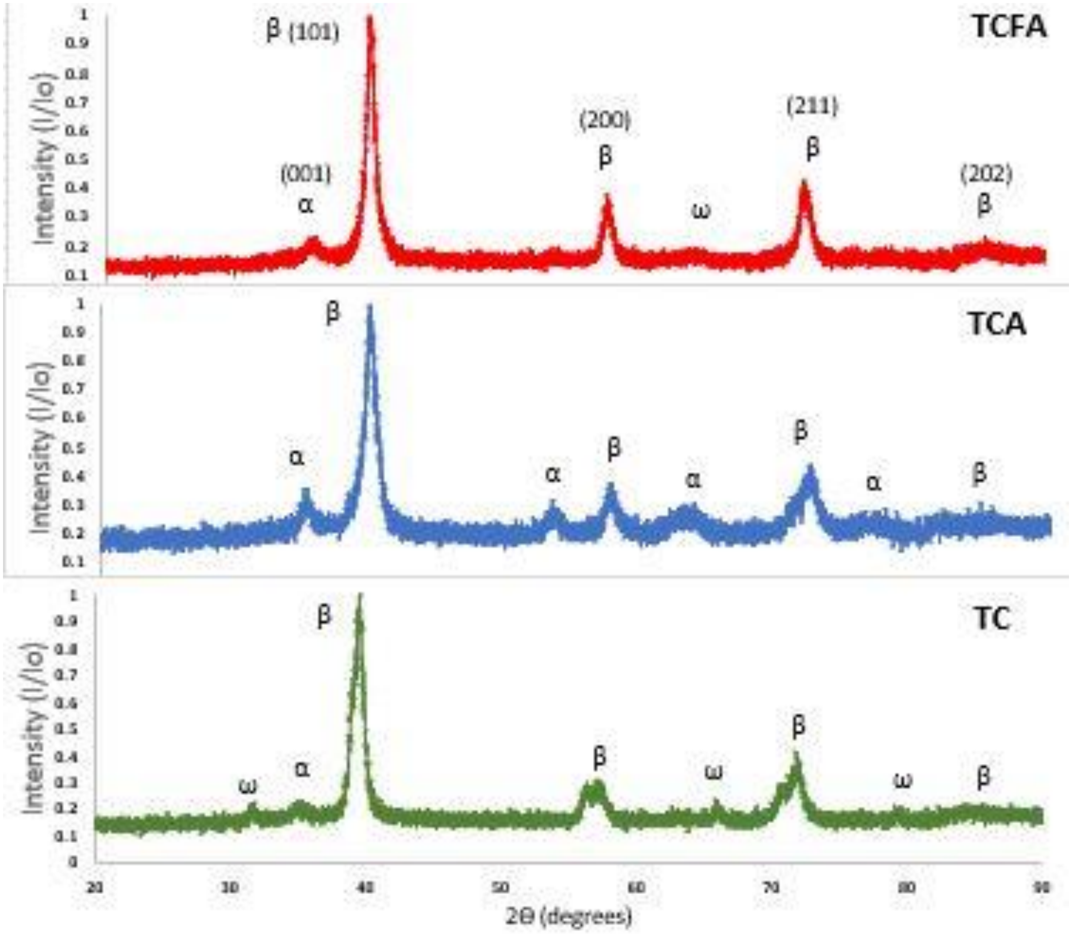

Figure 3. 2 XRD data in the form of Integrated intensity vs 2θ for the studied alloys HT at 683 K for 12 hrs

TC alloy showed larger number of ω-phase peaks compared to TCA and TCFA alloys. The presence of Al which is an α-phase stabilizer appears to have reduced the number of ω -phase peaks in the TCA alloy. It appears that the further addition of Fe to TCA has reduced the number and the intensity of the ω-phase peaks. Fe being a β-phase stabilizer could possibly reduce the amount of the ω-phase precipitation at this temperature. The aging duration could also play an important role in the number of secondary phase peaks and their intensities. The XRD pattern indicates the possible precipitation of both the ω and α-phases similar to what was reported by

Li et al. after isothermal aging of Ti-29Nb-13Ta-4.6Zr (wt. %) for 48 hrs between 573 K to 673 K (Li *et al.*, 2015).

The XRD patterns of the post-creep tested samples is indicated in Figure 3.3. The results showed peaks corresponding to the α, ω, and $TiCr_2$ phases. The intensity of the α peaks were higher for TCA compared to both TC and TCFA, which could be due to the presence of Al which is an α-phase stabilizer. The further addition of Fe seems to have reduced the α-phase peak intensity. The presence of the ω-phase has been reported to be the possible cause for the nucleation of the α-phase (Williams and Blackburn, 1969; Rhodes and Williams, 1975; Pennock, Flower and West, 1980; Azimzadeh and Rack, 1998; Ohmori *et al.*, 2001; Prima *et al.*, 2006; Nag *et al.*, 2009b; Li *et al.*, 2015) .

$TiCr_2$ intermetallic phase has been observed in other Ti-Cr alloys with higher concentrations of Cr. B. Martin found $TiCr_2$ lave precipitates in Ti-xCr (wt%.) alloys for Cr content between 12-15 wt.% aged between 773 K and 898 K (Martin, 2017). SEM imaging of Ti-15Cr (%wt.) initially showed sluggish precipitation of the $TiCr_2$ Laves phase at lower aging temperatures of about 843 K (Martin, 2017). Higher temperatures observed the Lave phases growing in clusters with the α phase both along grain boundaries and inside the grain (Martin, 2017).

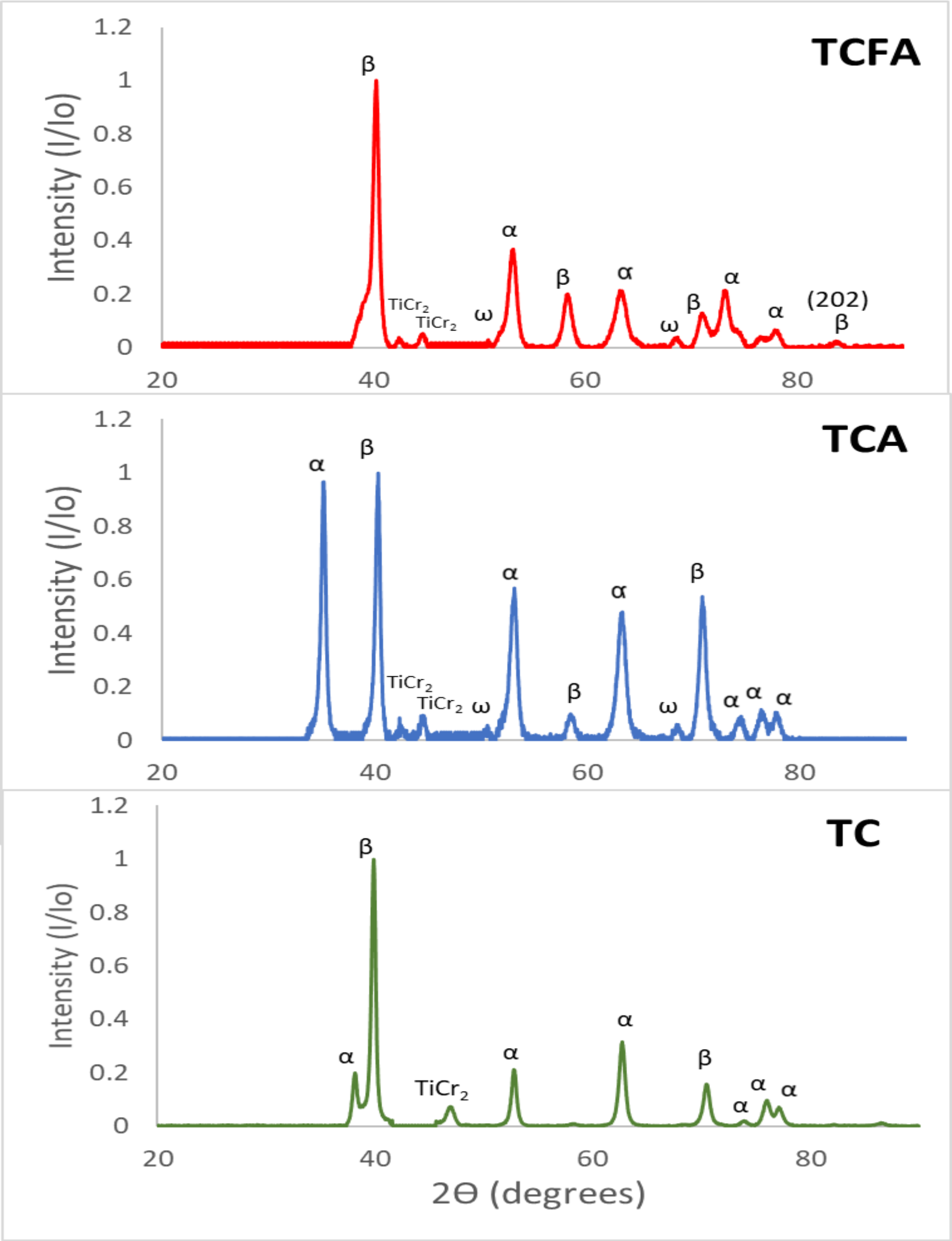

Figure 3. 3 XRD data in the form of Integrated intensity vs 2θ for the creep samples tested at 350 MPa and 683 K.

The XRD patterns of the TCFA alloy heat treated at 683K, 623 K, 573 K, and 483 K, for about 12 hrs is shown in Figure 3.4.

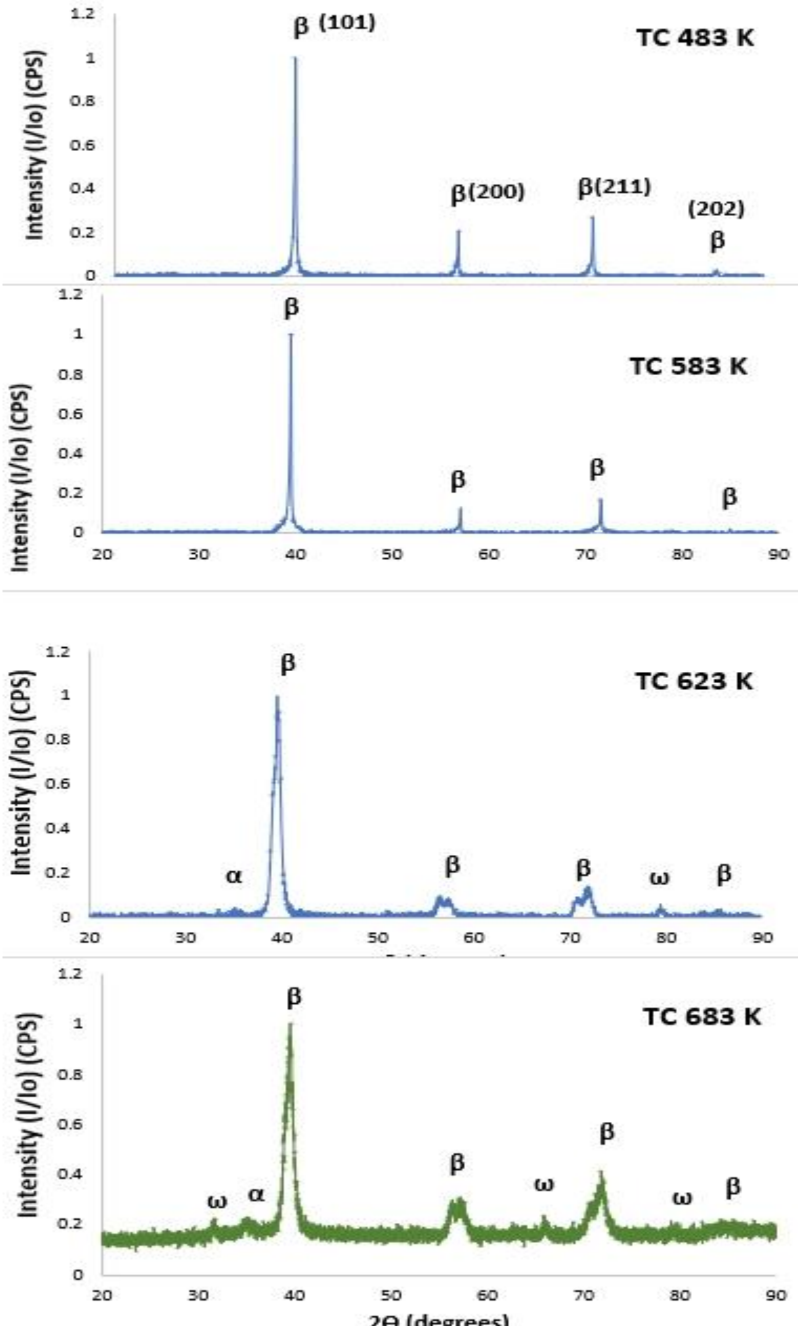

Figure 3. 4 XRD data in the form of Integrated intensity vs 2θ for the TC samples heat treated at 483 K, 583 K, 623 K, and 683 K and for 12 hrs

The XRD patterns for 483 K and 583 K showed only β-phase peaks. For higher heat treatment temperatures like 623 K and 683 K, the XRD pattern showed peaks corresponding to α-phase and ω-phase. The ω-phase forms during aging process for aging temperatures between 373 K and 773 K in β-Ti alloys (Hickman, 1969). The temperature versus aging time diagram for Ti-20V showed that the ω-phase formed at lower temperatures and for longer aging times for Ti-20V. The aging time of 12 hrs might not have been enough to nucleate the ω-phase or the α-phase for lower aging temperatures like 483 K and 583 K. Several studies have shown that α and ω-phases nucleate in β-Ti alloys for aging temperatures ranging between 573 K and 773 K and for aging temperatures ranging between 48 hrs to 100 hrs (Liu and Welsch, 1988; Li et al., 2002). The observed to α-phase and ω-phase peaks in Figure 3.4 for aging temperatures 623 K and 683 K are in line with the studies. Similar trends were observed for the TCA and the TCFA alloys.

In Figure 3. 5 the β-phase peaks for the as-processed, HT, and creep tested conditions were lined up in order to better visualize the secondary phase peaks in the alloys. The XRD patterns of the samples after HT for 12 hrs at 683 K indicates possible ω and/or α-phase peaks for the alloys. The XRD patterns of the post-creep tested alloys indicates peaks corresponding to the α, ω, and $TiCr_2$ phases. A larger number of α-phase peaks were observed in the creep tested samples as compared to the HT samples. It has been well documented that the α-phase nucleates from the ω-phase (Rhodes and Williams, 1975; Pennock, Flower and West, 1980; Azimzadeh and Rack, 1998; Ohmori et al., 2001; Prima et al., 2006; Nag et al., 2009b; Chen et al., 2014). It is possible that during creep deformation, the α-phase nucleated from the ω-phase which could explain the peaks observed in figures. For the TC alloy, peak splitting of the β (200) and β (101) peaks were observed after HT and in the creep tested conditions, whose cause is not understood yet. For TCA and TCFA alloys, β (211) and β (202) peaks do not show up in the XRD plots in the after creep tested condition which is unusual and not completely understood.

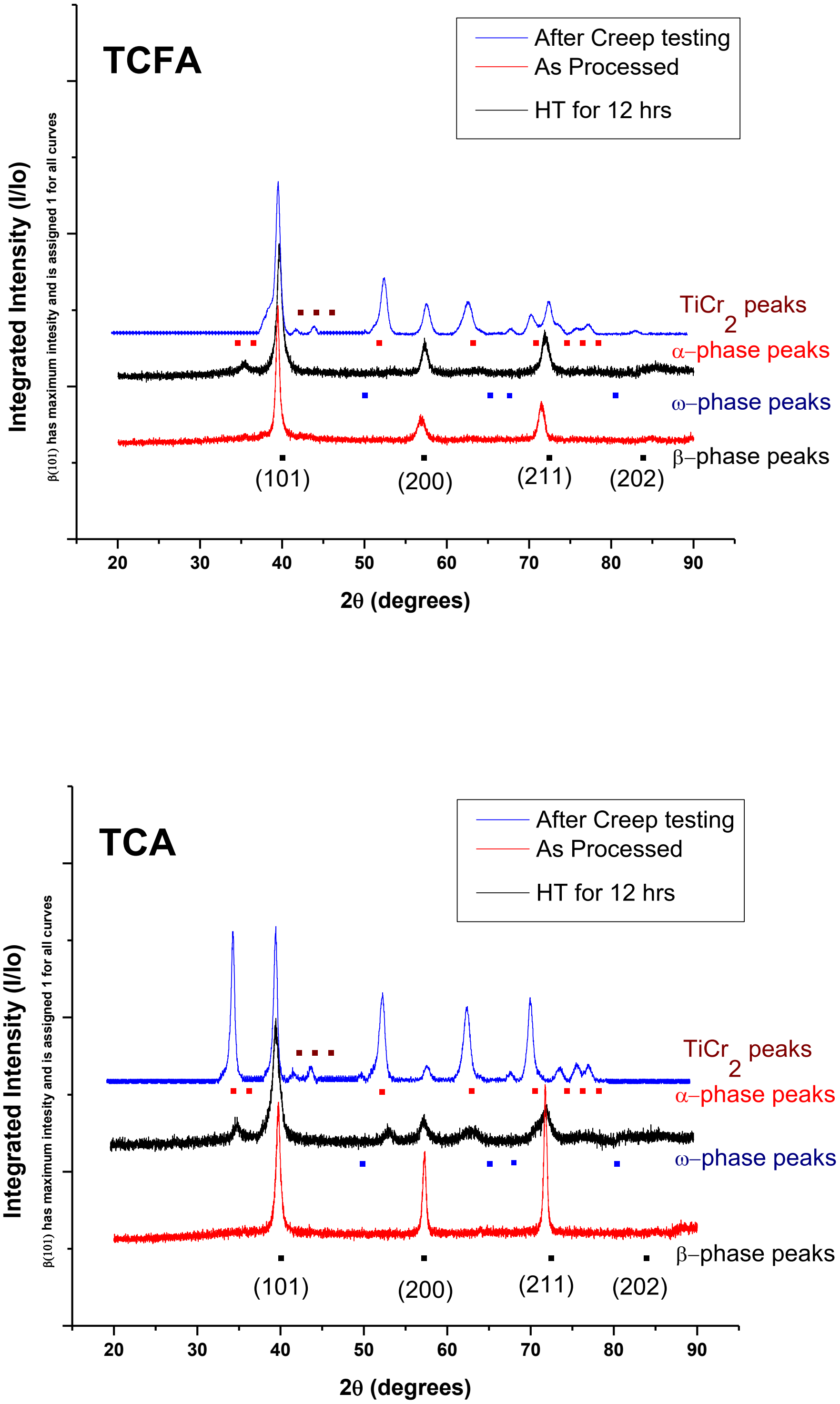

Figure 3. 5 XRD plots comparing as-processed, HT, and creep tested conditions.

Figure 3. 5(cont'd)

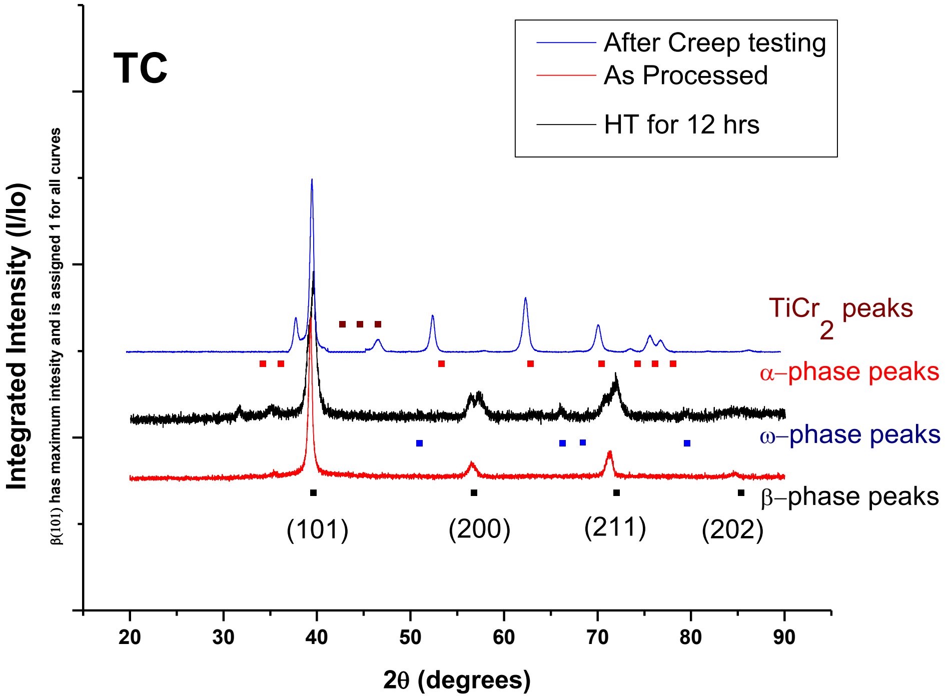

3.1.2 SEM results

Figures 3.6 shows the microstructures of the alloys in the as-processed condition. The BSE photomicrographs of the cross section of the as-processed samples reveals a β-phase microstructure. Figure 3.7 shows the microstructures of the cross section of grips of the alloys after creep testing at 350 MPa and 683 K. The grip section of the creep tested samples was only subjected to about half the stress that the gage section experienced for about 13 days (~ 2:1 is ratio of areas of the grip and gage sections).

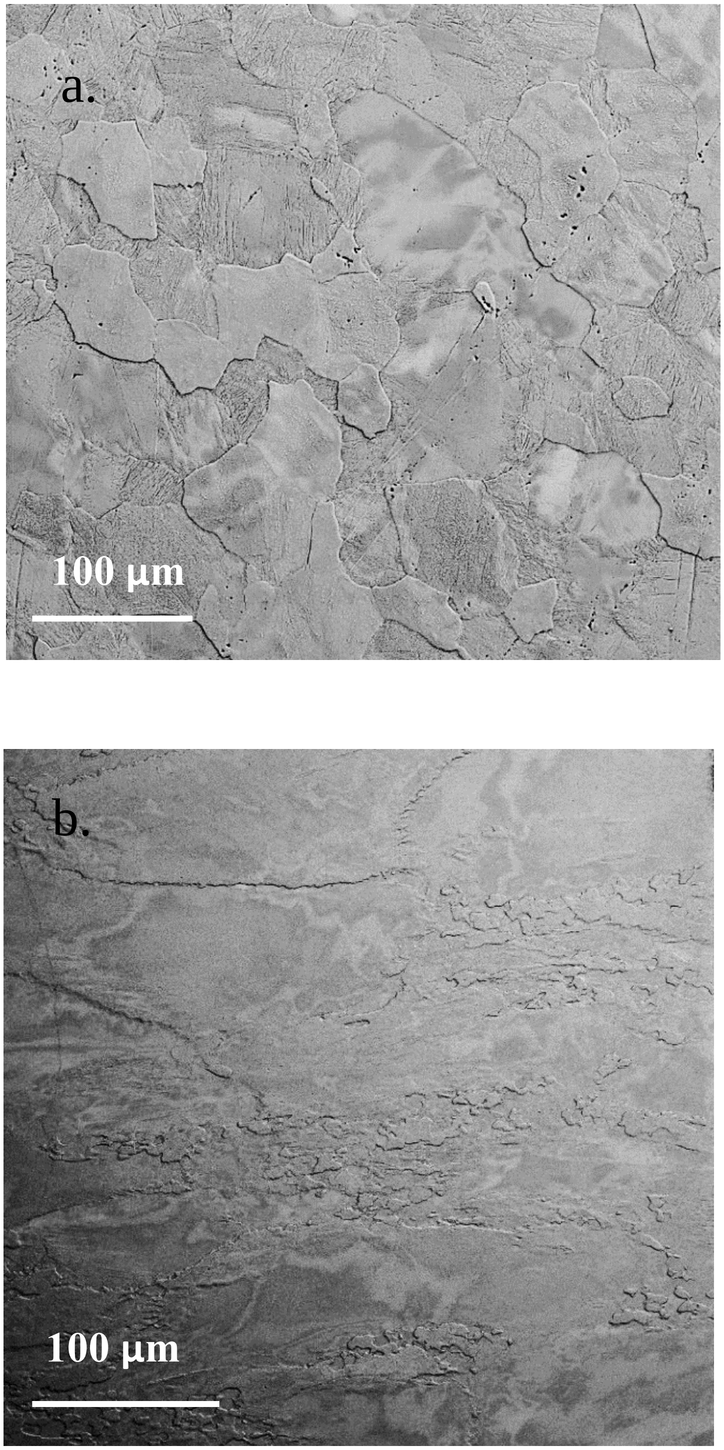

Figure 3. 6 BSE SEM photomicrographs of the cross section of the as-processed microstructures of a.) TC b.) TCA and c.) TCFA alloys. Samples were etched using Kroll’s reagent.

Figure 3. 6 (cont'd)

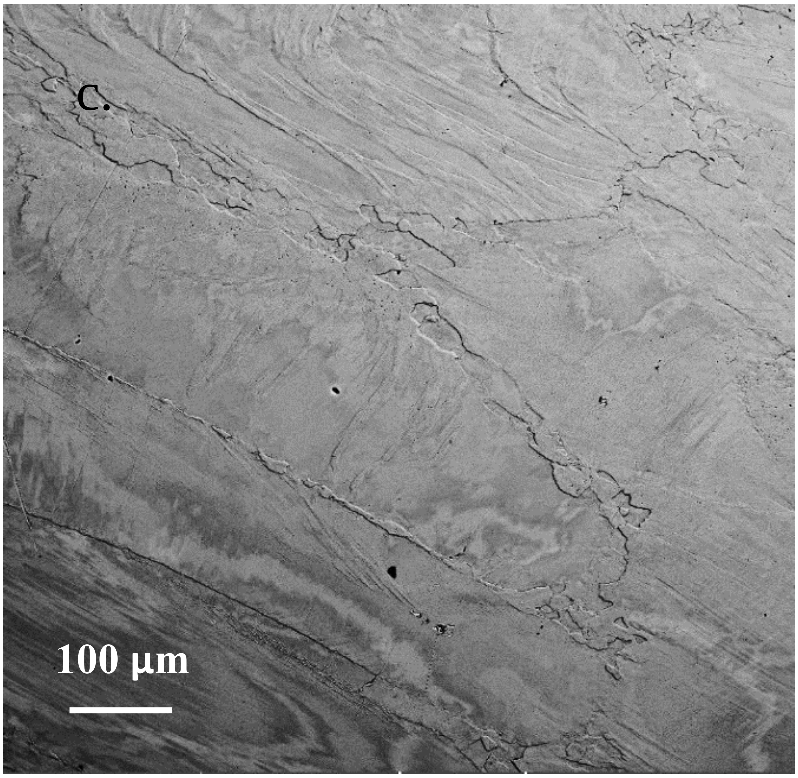

In the as-processed alloys, the addition of Al increased the grain size almost by a factor of 1.4 compared to the TC alloy. The addition of both Fe and Al only resulted in a very comparable grain size value compared to the TC alloy. The addition of Al alone had a more pronounced effect on the grain size.

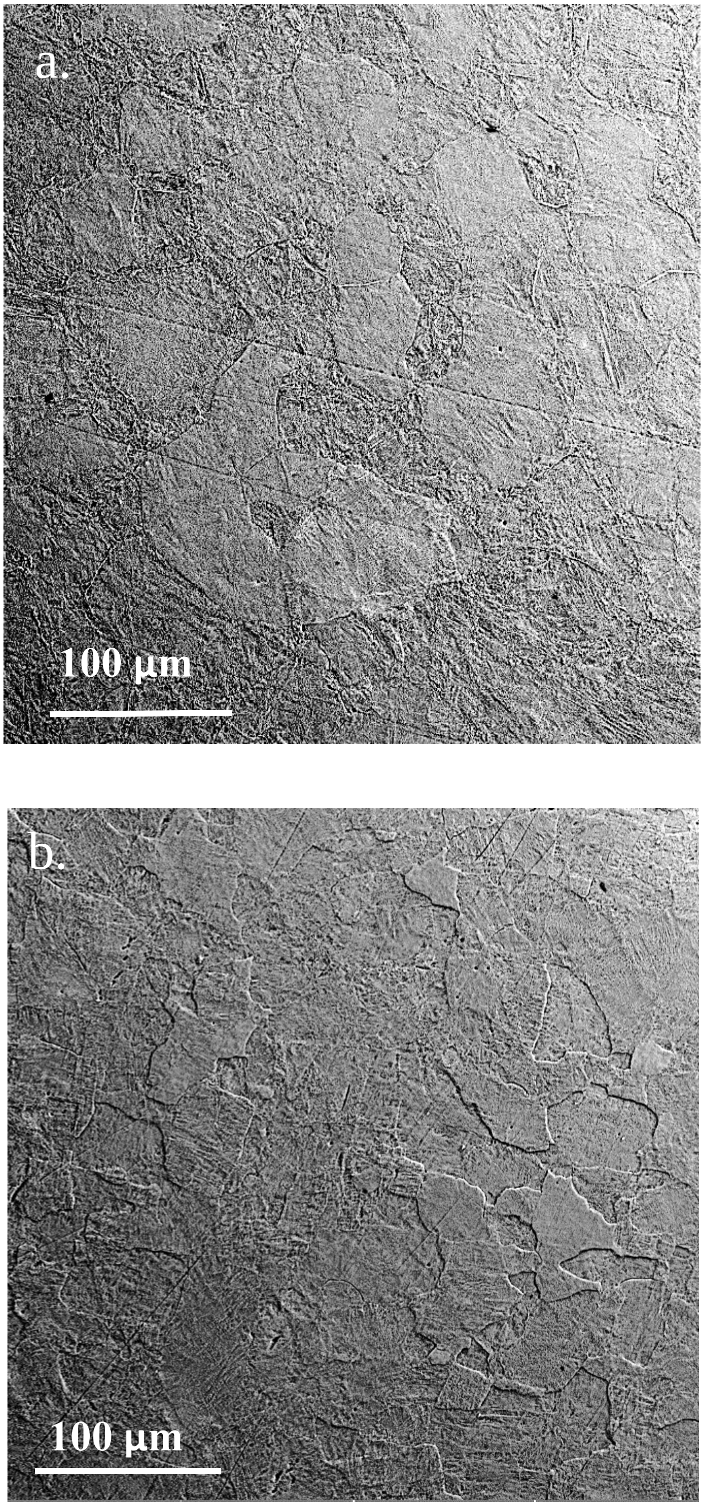

Figure 3. 7 BSE SEM photomicrographs of the microstructures of a.) TC b.) TCA and c.) TCFA alloys taken from the cross section of the grips of creep tested samples and etched.

Figure 3. 7 (cont’d)

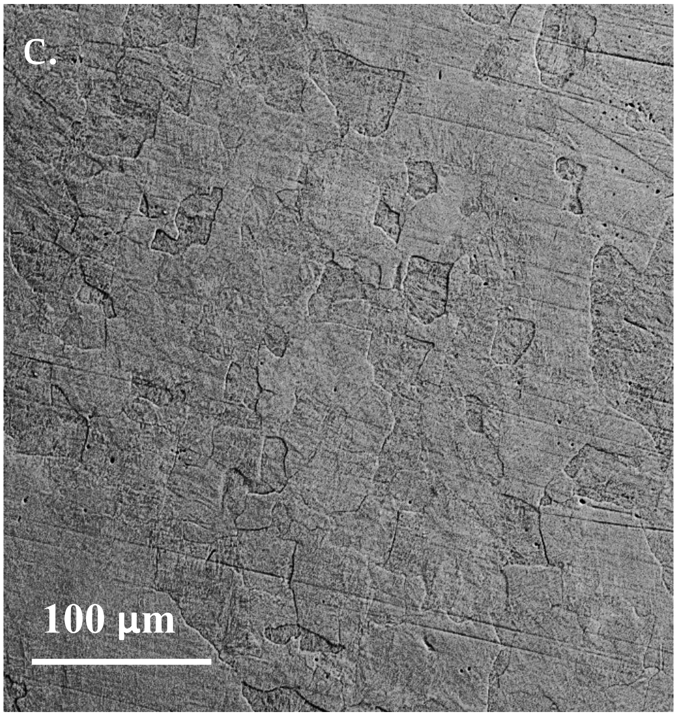

The average grain size for β phase in the as- processed condition was compared with the grain sizes from grips of the creep tested samples. For the grips of the creep tested samples, the average β-phase grain size was comparable.

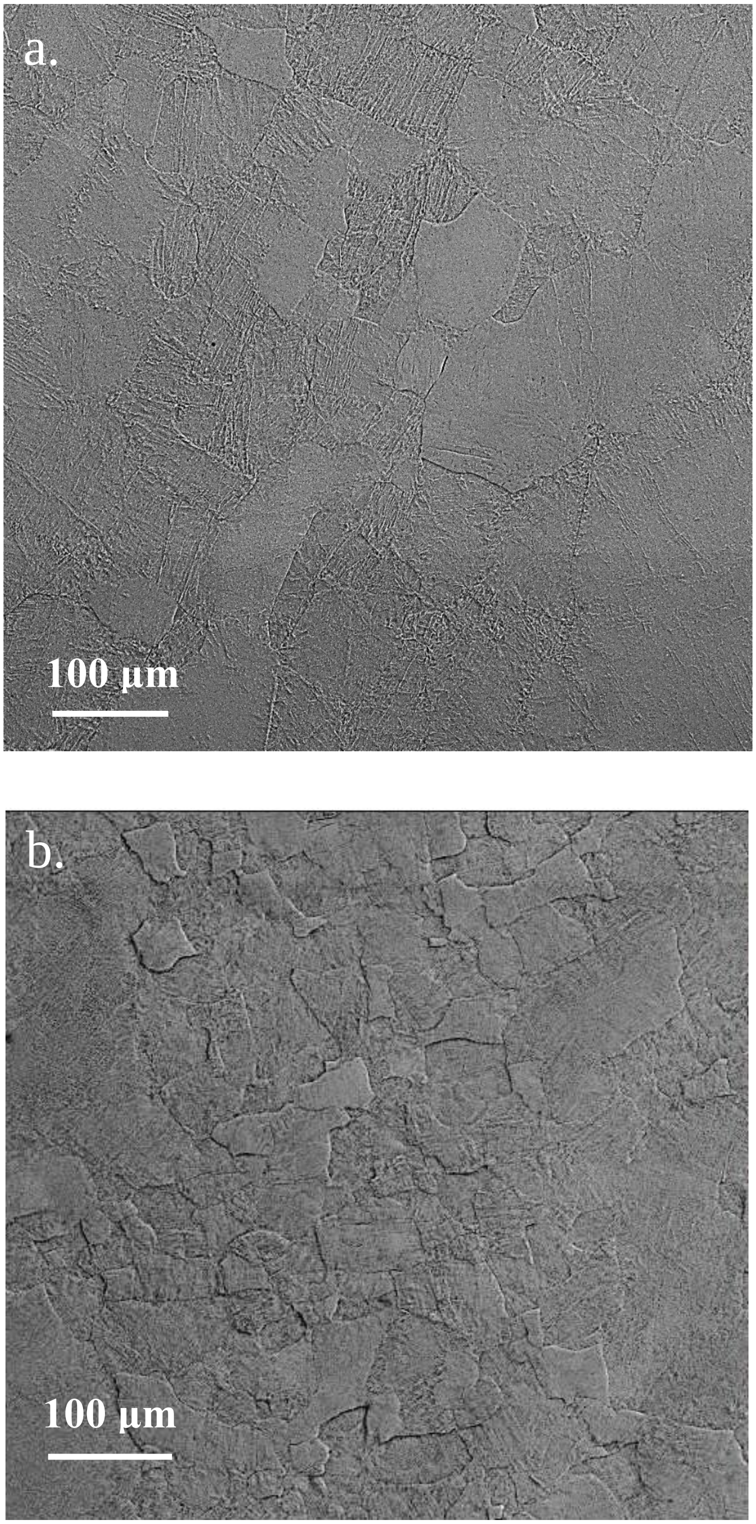

Figure 3. 8 BSE SEM photomicrographs of the microstructures of a.) TC b.) TCA and c.) TCFA alloys taken from the cross section of the gage of samples creep tested at 350 MPa and 583 K

Figure 3.8 (cont'd)

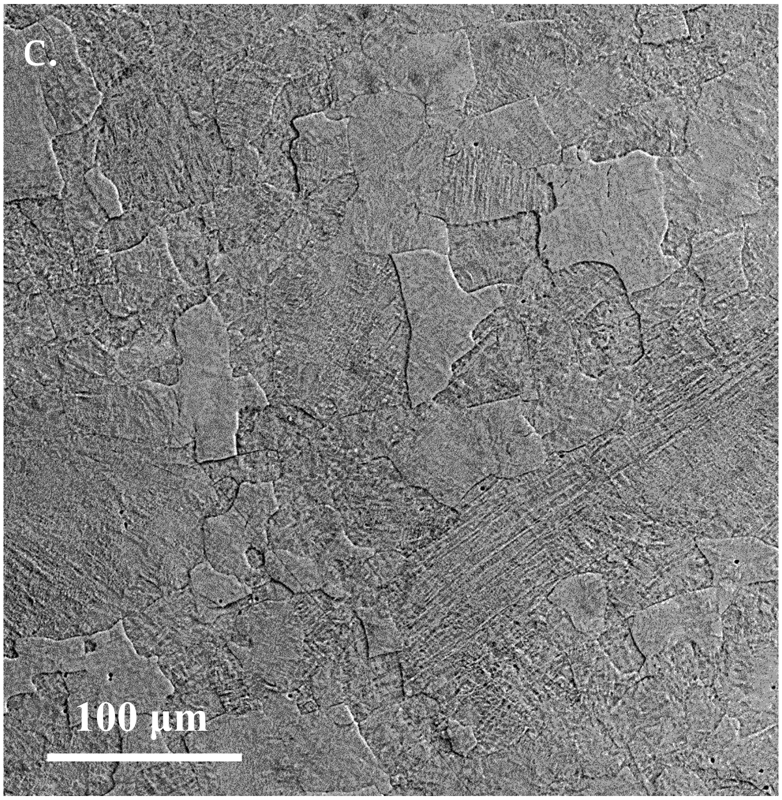

Figure 3.8 shows the microstructures of the cross section of gage of the alloys after creep testing at 350 MPa and 683 K for about 13 days. The TC grain size was comparable in the grip, gage section, and in the as-processed conditions. Table 3.1 summaries the observed grain size results.

The observed decrease, after creep testing compared to the as-processed condition, may be due to the possible phase transformations occurring during creep in the gage section. All the observed grain size changes were within a factor of 2 for the studied alloys going from the as-processed to the creep tested conditions. TC exhibited the largest grain size while TCFA exhibited the smallest grain size after creep.

Table 3. 1 Summary of the grain sizes of the as-processed (BCC) and creep tested (transformed BCC) microstructures

	Average grain size (μm)		
	TC	TCA	TCFA
As-processed :	60.2		
Elongated direction		135.5	84.1
Transverse direction		64	58.8
Heat treated (grip section post creep)	57.7	54.4	55.8
Creep tested in the gage section	56.1	41.4	36.4

Representative BSE SEM images of the as-processed alloys are provided in Figure 3.9. The SE SEM images for the creep tested gage section are provided in Figure 3.10. The SE images show pit-like nanoscale structures with visible topographical contrast suggesting possible secondary phase(s). Based on the XRD results which show the presence of α-phase ω-phase, it is expected that these fine features in Figure 3.10 were α and/or ω precipitates. Future Transmission electron microscopy (TEM) analysis is intended to verify the phase(s) observed.

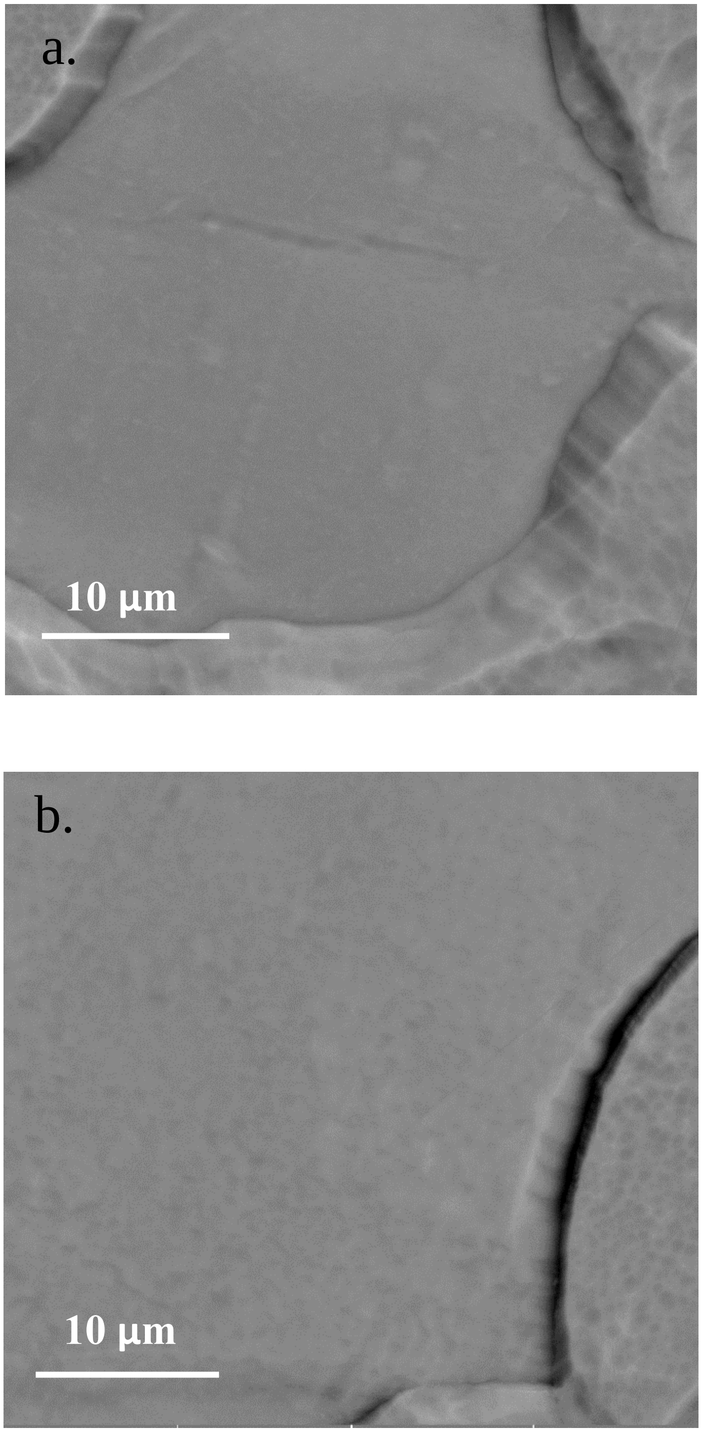

Figure 3. 9 BSE SEM photomicrographs of the as-processed a.) TC, b.) TCA, and c.) TCFA alloys. Samples were etched using Kroll’s reagent

Figure 3. 9 (cont'd)

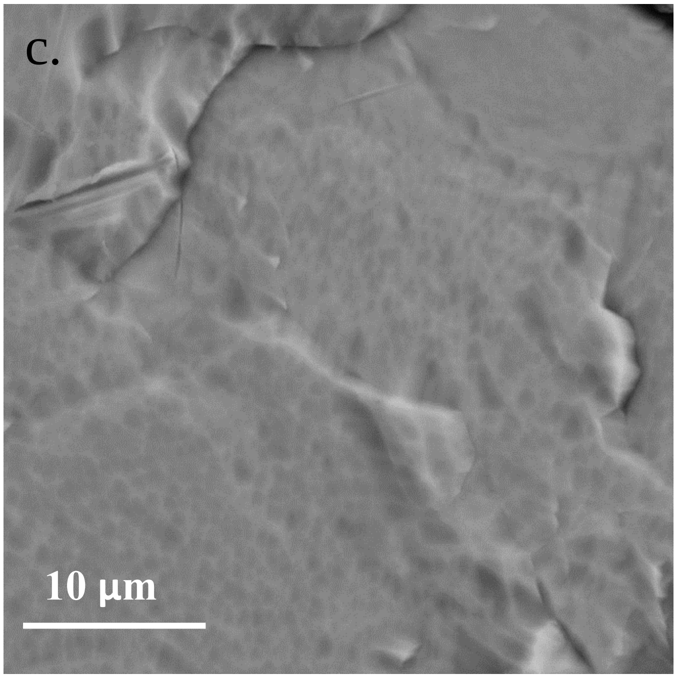

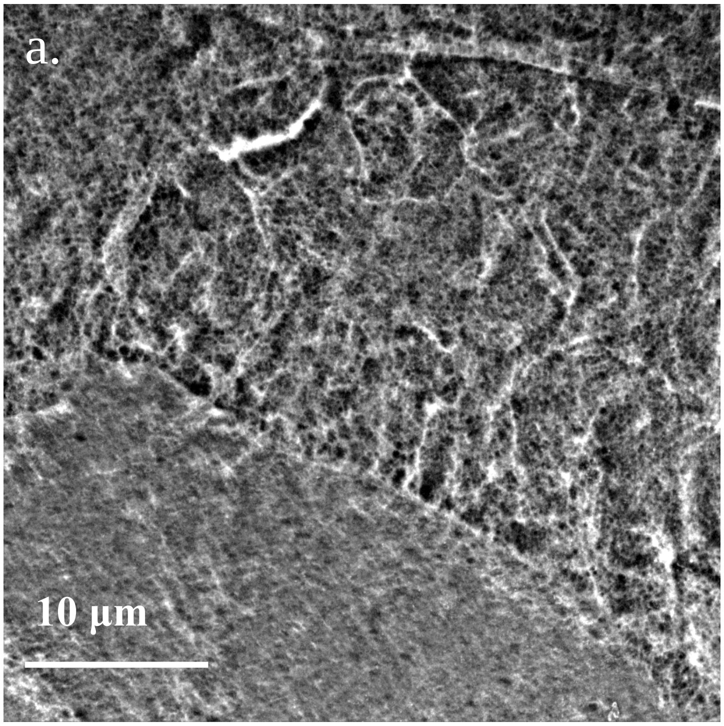

Figure 3. 10 SE SEM photomicrographs of a.) TC, b.) TCA, and c.) TCFA alloys after creep testing at 350 MPa exhibiting the β phase matrix with pit-like structures indicating presence of secondary phase(s). Samples were etched using Kroll's reagent

Figure 3. 10 (cont’d)

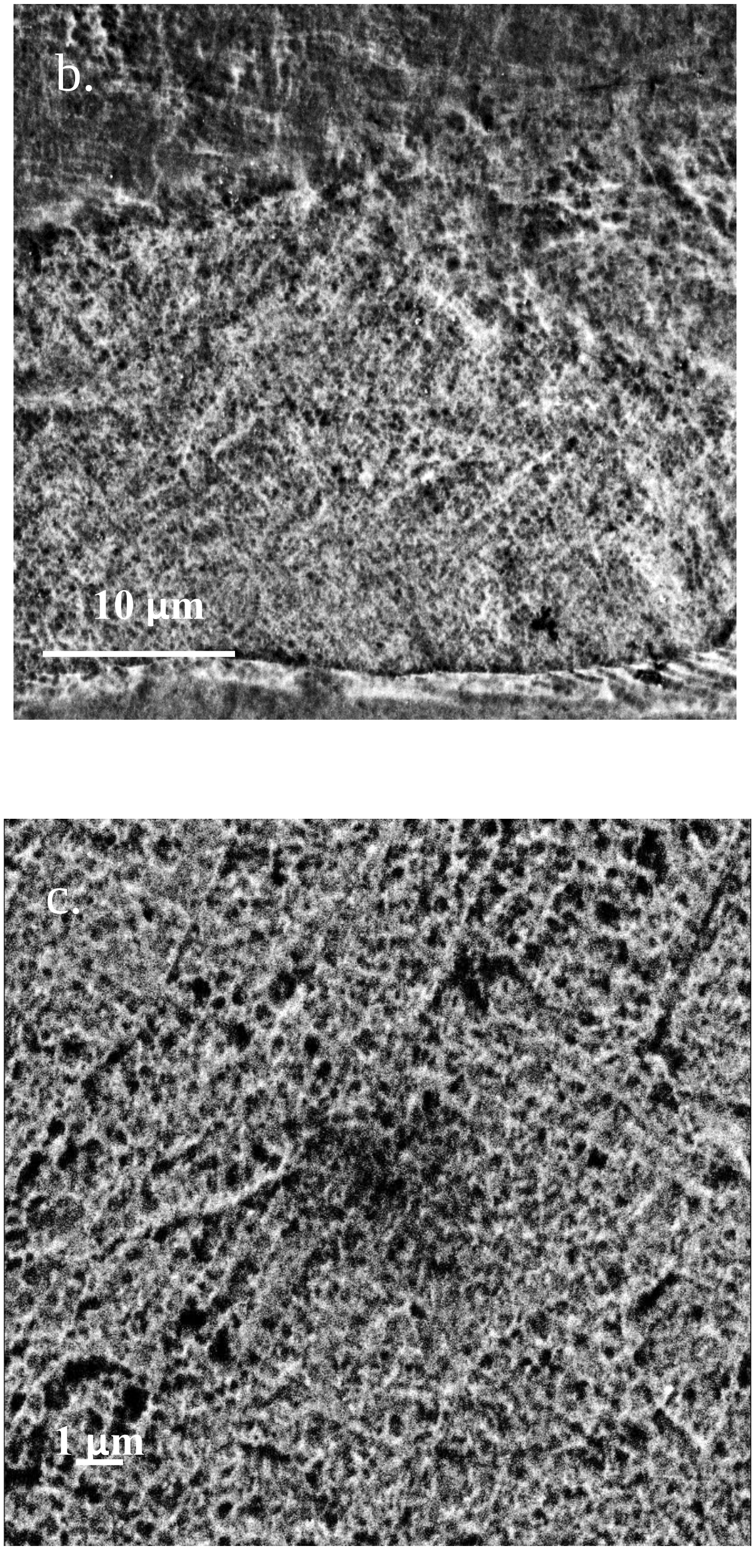

The volume fraction of the precipitates in the alloys were evaluated from BSE photomicrographs using the thresholding function in the image editing software ImageJ as shown in Figure 3.11. TC and TCA showed similar values of 59.7 % and 59.1 % respectively for the precipitate volume fraction (see Table 3.2).

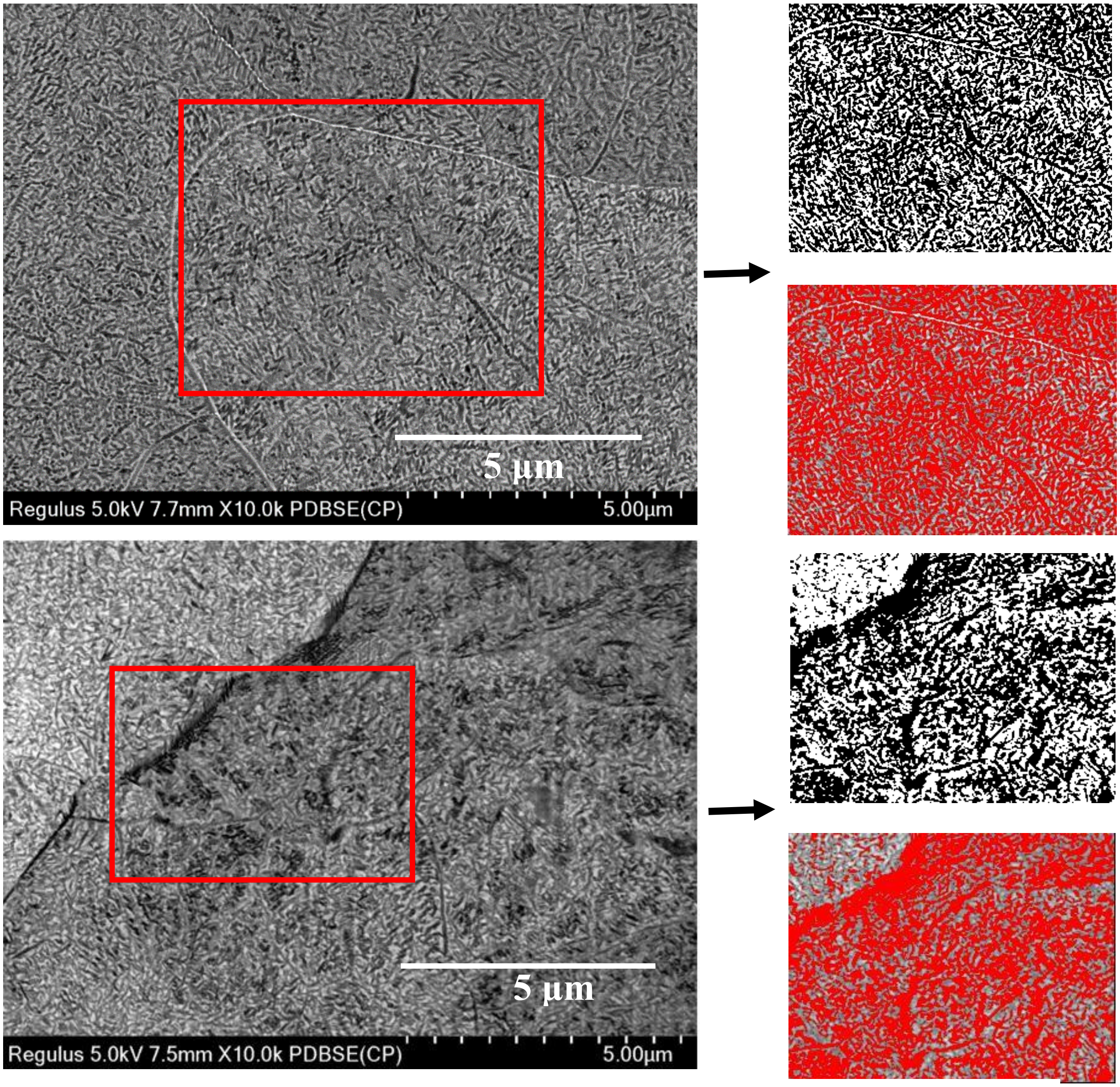

Figure 3. 11 BSE SEM photomicrographs of a.) TC, b.) TCA, c.) TCFA alloys with corresponding ImageJ contrast and thresholding images.

Figure 3. 11 (cont’d)

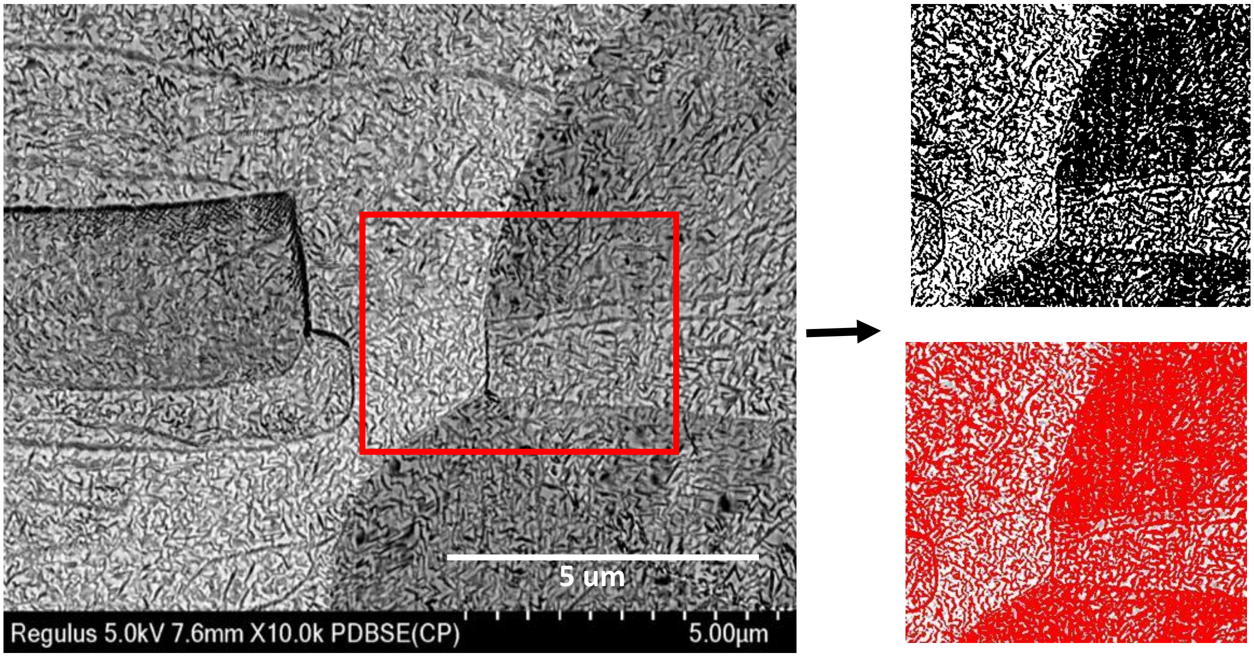

As such, there seems to be a reduced effect of Al on the precipitate volume fraction. TCFA had a higher precipitate volume fraction of 63.1 %. The addition of Fe and Al to TC showed an increase of about 6 % in the precipitate volume fraction compared to TC alloy. The higher precipitate fraction in TCFA could possibly be the cause for greater creep resistance compared to the other two alloys.

Table 3. 2 Summary of precipitate volume fractions of the alloys

Alloys	Trials	Mean volume percent of precipitates (%)	Mean volume percent of bulk (%)	Minimum	Median	Maximum
TC	6	**59.7**	**40.3**	57.2	59.2	64.5
TCA	5	**59.1**	**40.9**	54.1	58.2	64.2
TCFA	5	**63.1**	**36.9**	61.1	63.1	65.2

3.2 Mechanical Properties

3.2.1 Vickers Hardness

The Vickers hardness testing and the results are represented in Figure 3.12. The alloys show an increase in the HV after creep testing. TCFA showed a 75% increase, followed by TCA with a 68%, and then by TC with a 50% increase. This could be due to the precipitation hardening effects observed in β-Ti alloys which strongly hinders the movement of dislocations. Due to the aging process, precipitates nucleate and change in volume fraction, size, and geometry leading to an increase in the strength and hardness of β-Ti alloy (Kobayashi *et al.*, 1998; Donachie, 2000; G Lütjering and Williams, 2003; Ivasishin *et al.*, 2003; Dehghan-Manshadi and Dippenaar, 2011; Chen *et al.*, 2014).

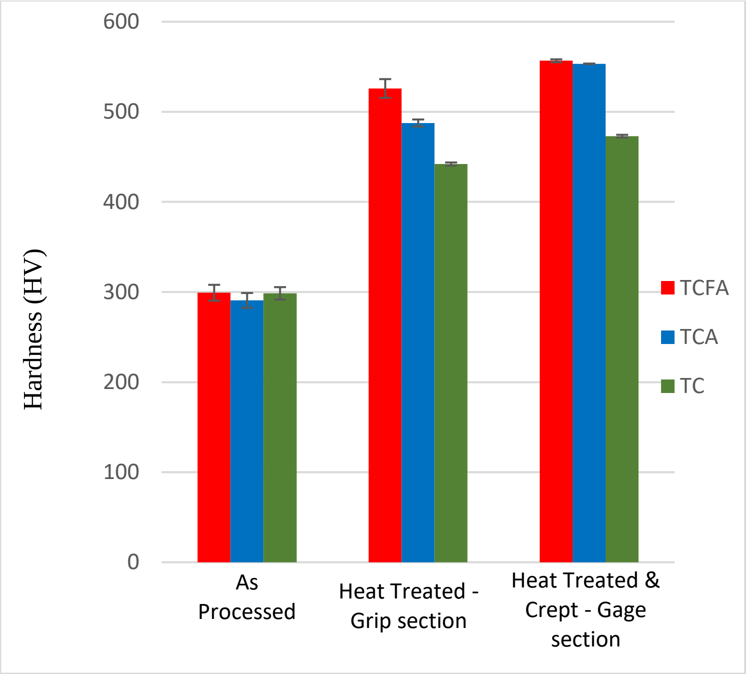

Figure 3. 12 Hardness values for the alloys in the different conditions showing an increase from as-processed to the heat-treated grip section and a further increase in the crept gage section

B.S. Hickman et al. found that the β-phase to ω-phase transformation occurs in the temperature range of 373 K and 773 K in β-Ti alloys (Hickman, 1969). The hardness values increase is likely a result of the ω and α-phase precipitate formation. The gage section hardness values were 5-10% larger than those in the grip section. This is expected to be a result of the increased dislocation content in the gage as compared to the grip.

The increase in the hardness values post creep could also be due to the presence of intermetallic $TiCr_2$ phase, observed in the previous XRD results, along with ω and α phase precipitates. B. Martin observed an increase in the hardness value from about 175 HV to 360 HV in Ti-xCr (wt.%) alloys as 'x' was varied from 1-15 wt.% Cr (Martin, 2017). This was attributed to the increase in α + $TiCr_2$ precipitation in the alloy with the increase in the Cr concentration (Martin, 2017). Chen et al. studied hardness in the Ti-Cr alloy space and observed the effects of ternary additions and two-phase binary alloys containing Ti-Cr (Chen, 1996). They found that formation of the Lave $TiCr_2$ phase in conjunction with a Ti-Cr bcc improved the toughness and the hardness of the alloy (Chen, 1996). The addition of ternary elements, like Mo, V, and Fe, increased the toughness of these alloys (Chen, 1996). This was explained by studies showing an improved ductility through dispersion and relaxation of the closed-packed structure on addition of ternary elements as substitutional solutes (Chen, 1996).

3.2.2 Creep tests results

The representative heating plots are shown for the alloys in Figure 3.13. A slight decrease was observed in the deflection and in turn the strain, initially at shorter heat treatment times, and the strain seemed to stabilize at longer heat treatment times. The initial drop in the strain value could be due to the phase transformations taking place in the alloys with heat treatment. Although each of the creep samples were heat treated at the creep temperature (683 K) for 48 hrs prior to loading (creep testing), it is possible that the phase transformations were not complete. Therefore, the microstructure may still have been evolving during the subsequent creep exposure.

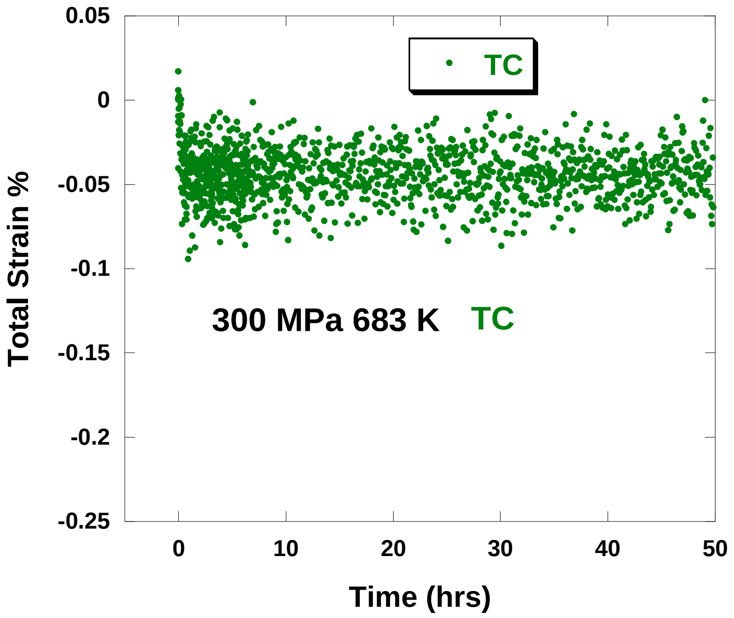

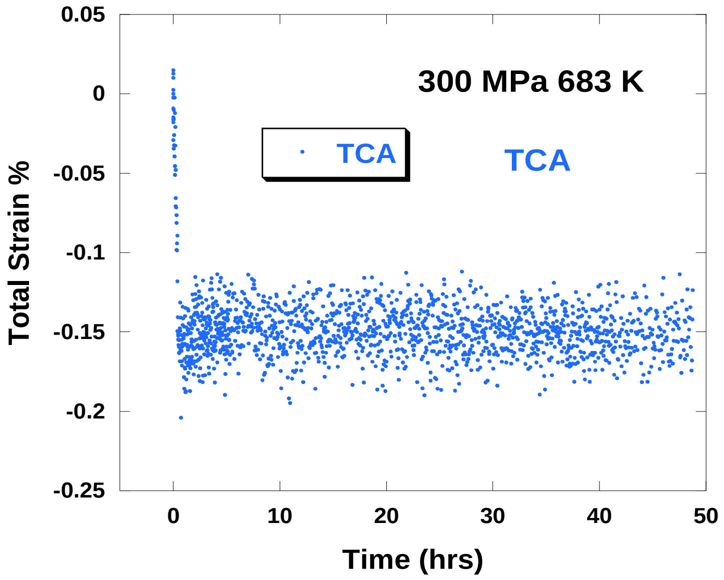

Figure 3. 13 Total Strain vs time heat treatment plots for a.) TC, b.) TCA, and c.) TCFA showing a slight drop in deflection at lower times and stable deflection at higher times.

Figure 3. 13 (cont'd)

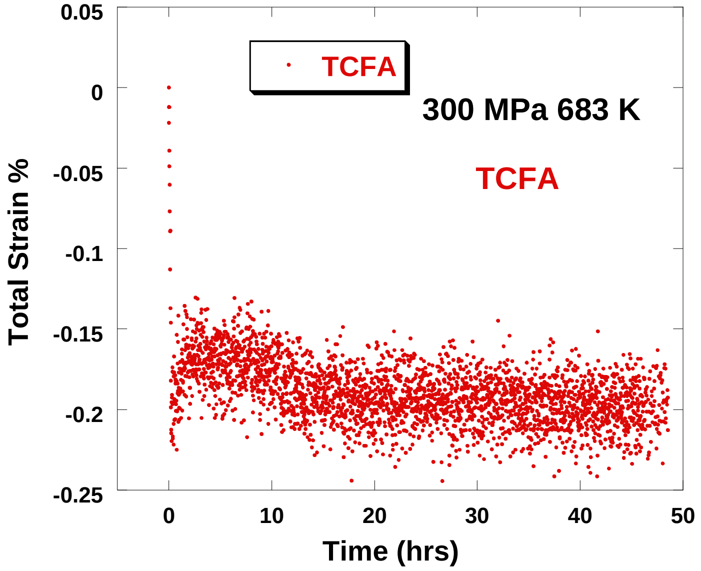

A summary of all the creep tests performed on the alloys, their conditions, and the results obtained can be found in Table 3.3.

Table 3. 3 Summary of creep tested specimens

Test Number	Material	Stress (MPa)	Creep temperature (K)	Creep test duration (hrs)	Total strain %	Creep Strain %	ε_{ssmin} (10^{-4}) (1/hr)
1	TCFA	350	683	306	1.59	1.38	3.4
2	TCA	350	683	342	2.49	2.14	2.7
3	TC	350	683	282	2.97	2.59	3.3
4	TCFA	300	683	645	2.42	2.22	1.5
5	TCA	300	683	645	2.42	1.65	2.1
6	TC	300	683	588	3.1	2.75	2.7
7	TCFA	250	683	890	1.91	1.82	1.4
8	TCA	250	683	442	1.65	1.48	1.9
9	TC	250	683	475	2.26	2.01	2.2
10	TCFA	200	683	617	0.85	0.78	0.6
11	TCA	200	683	162	0.88	0.69	0.4
12	TC	200	683	432	2.14	1.94	1.9

The strain rate vs time for the TCFA alloy creep tested at 350 MPa and 683 K displayed a strain rate curve plateauing with increasing time indicating secondary creep regime and a steady state creep rate (see Figure 3.14). The plot is representative of all the samples creep tested, and the creep tests were stopped in the secondary creep regime.

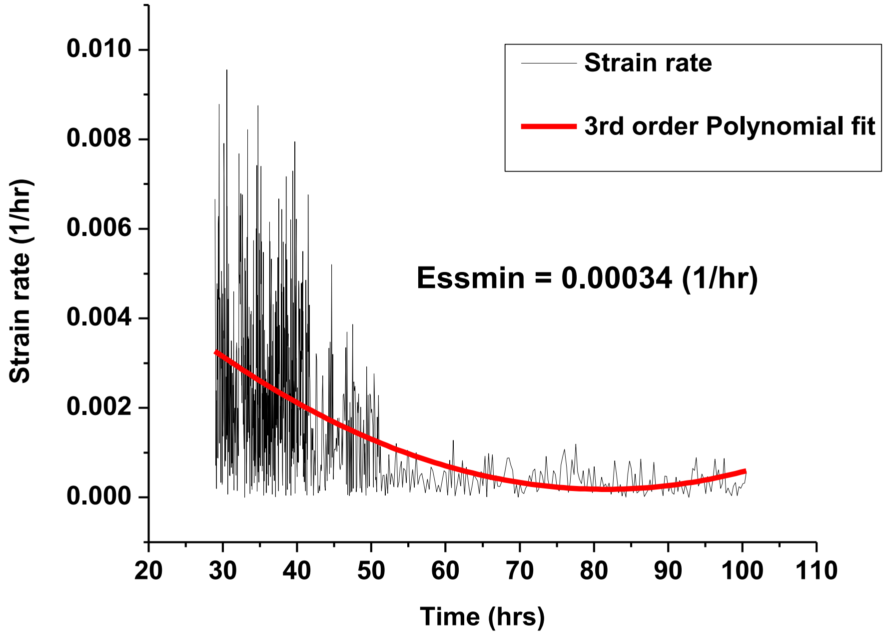

Figure 3. 14 Representative strain rate vs time plot for TCFA alloy at 350 MPa and 683 K displaying a plateauing of strain rate curve with increasing time indicating secondary creep regime. The plot is representative of all the creep experiments.

Figure 3.15 compares the creep strain vs time curves for TCFA as a function of applied stress at 683 K. The curves indicate an increase in the creep strain as the stress was increased. Similar trends were observed for the other two alloys.

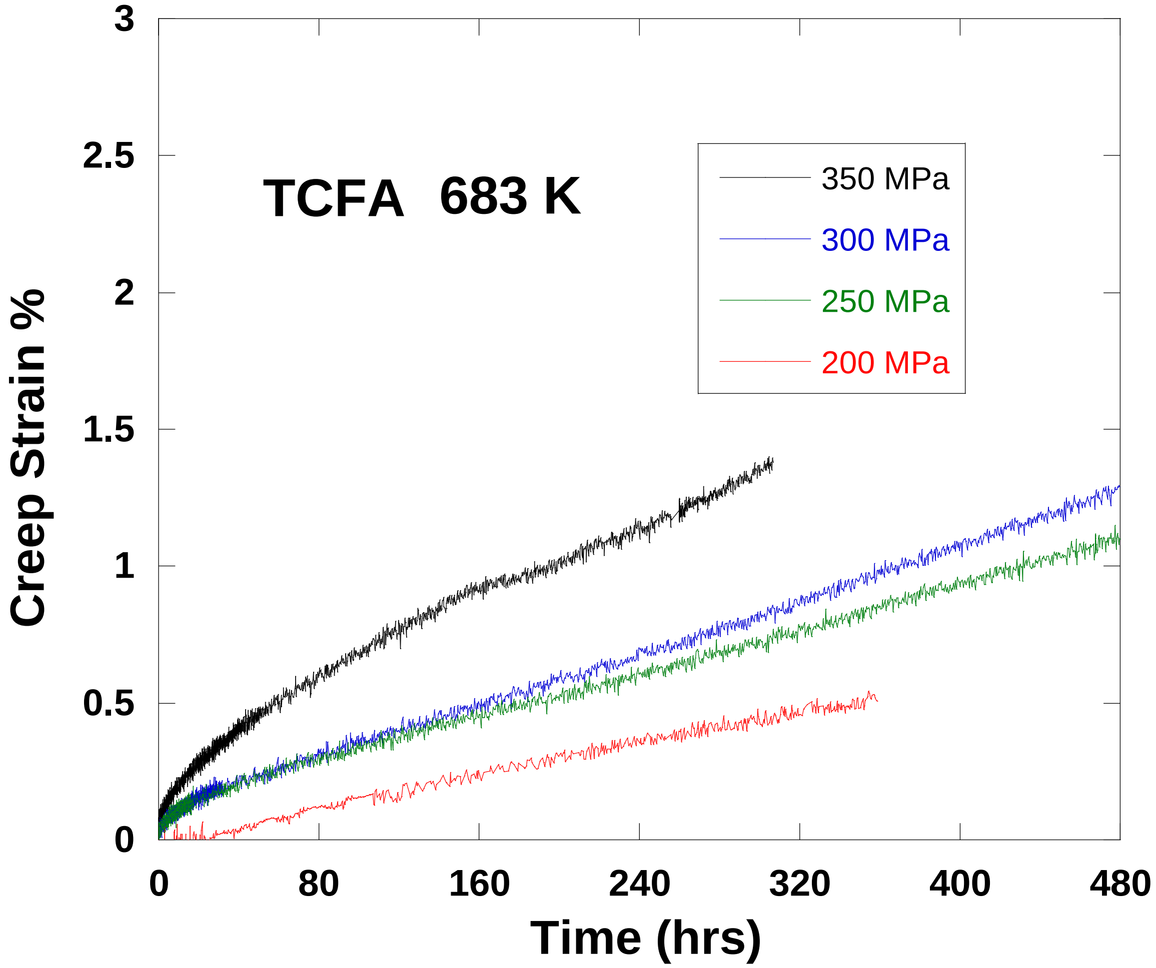

Figure 3. 15 Creep strain vs time plots for TCFA alloy at 683 K and varying applied stress levels

Figure 3. 16 compares the creep stain versus time plots for the three alloys at each of the applied stress levels. At 200 MPa, TCFA exhibited greater creep resistance followed by TCA and then TC as observed in Figure 3. 16. This trend in the creep resistances was consistently seen over all the four applied stress values. This indicates that the addition of both 3 wt. % Al and 1 wt. % Fe to Ti-12Cr (wt. %) provided the greatest creep properties among the alloys

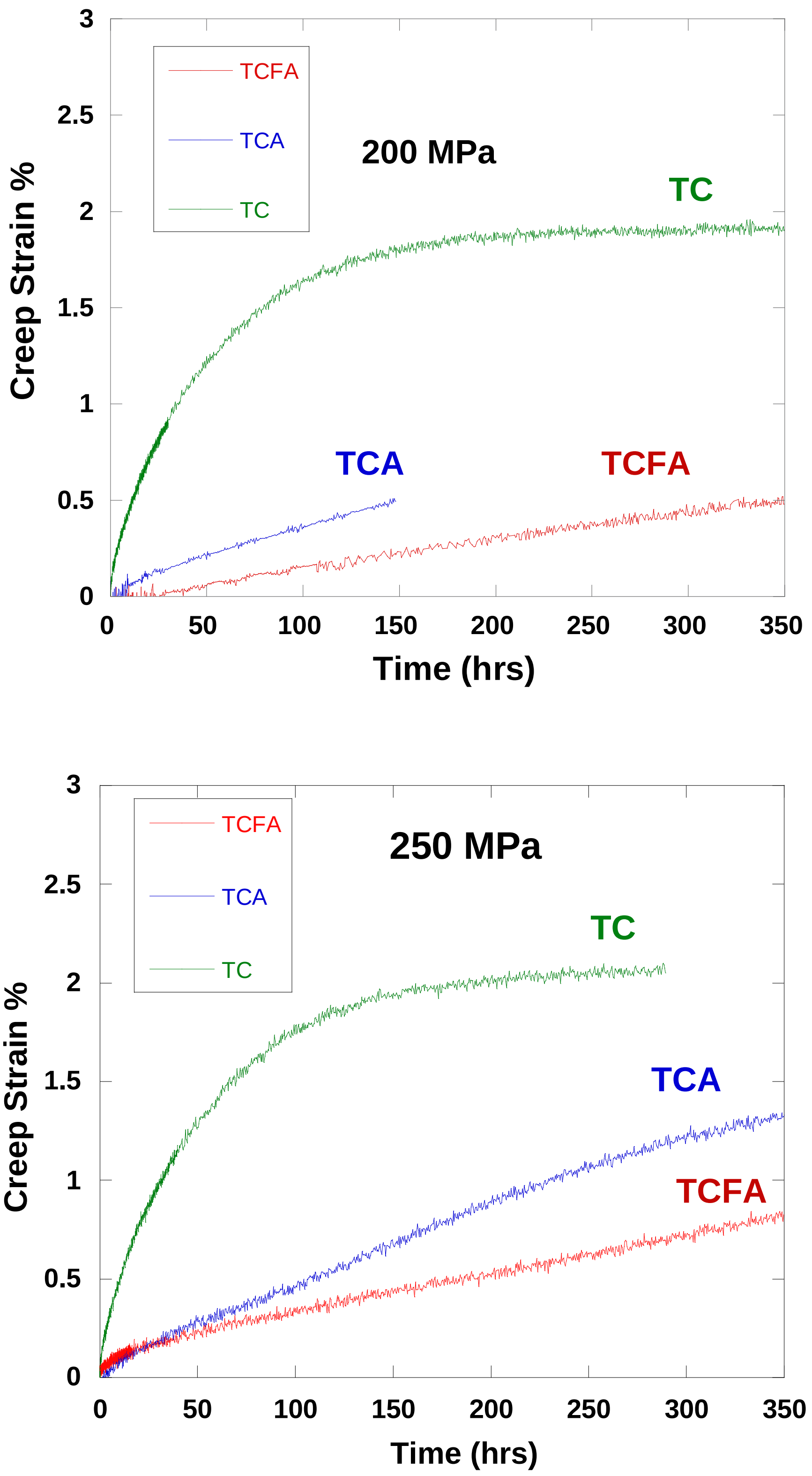

Figure 3. 16 Creep strain vs time plots for the three alloys tested at 683 K and a.) 200 MPa, b.) 250MPa, c.) 300 MPa, d.) 350 MPa showing a consistent creep resistance trend.

Figure 3. 16 (cont'd)

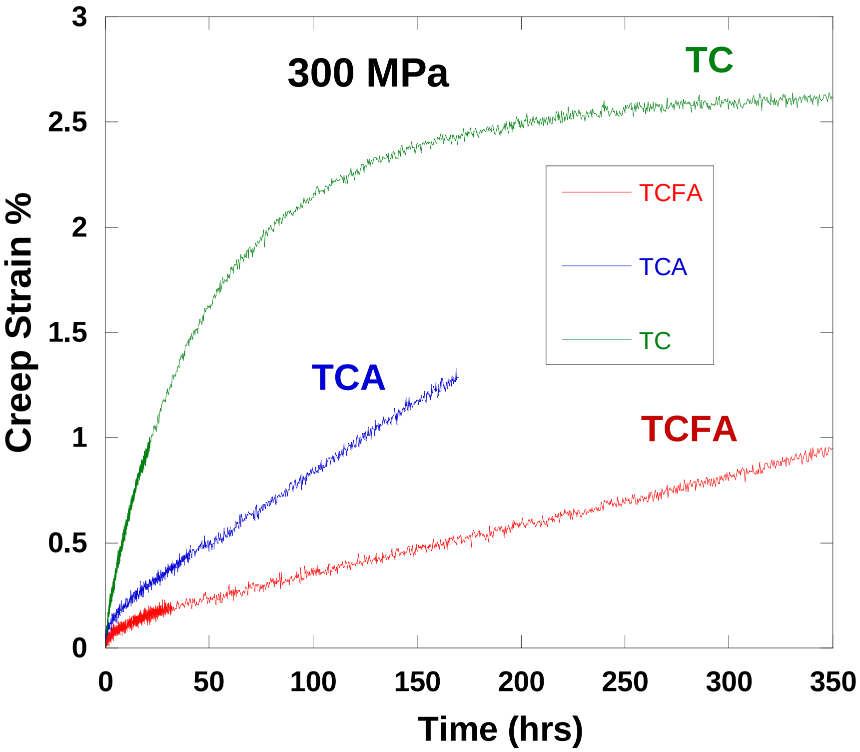

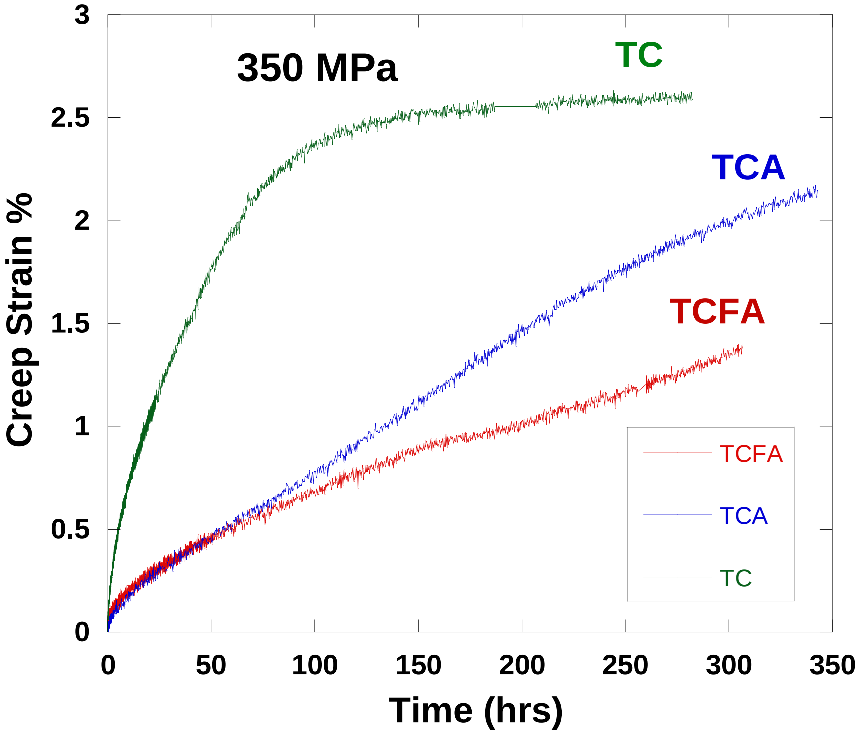

The creep strain vs time plots for TCFA alloy tested at 350 MPa and 683 K, before and after heat treatment, were compared with Ti-6Al-4V tested at 350 MPa and 673 K (see Figure 3.17).

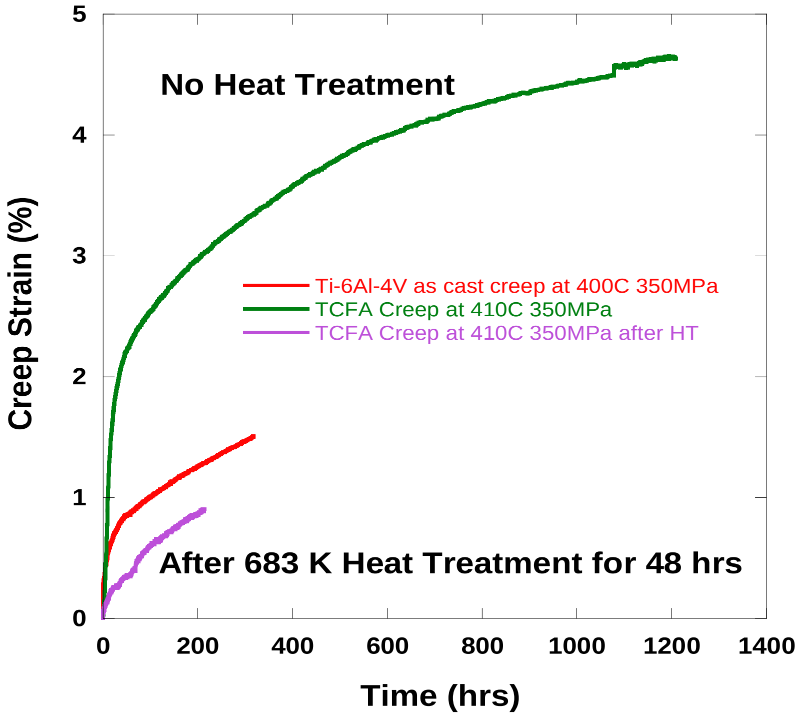

Figure 3. 17 Comparison creep strain vs time plot for TCFA alloy tested at 683 K and 350 MPa before and after heat treatment, with Ti-6Al-4V tested at similar conditions.

TCFA exhibited greater creep resistance than Ti-6Al-4V after heat treatment at 683 K for 48 hrs prior to creep testing. TCFA alloy with no prior heat treatment exhibited lesser creep resistance than Ti-6Al-4V. This could indicate that after the β to ω-phase transformation, the TCFA alloy exhibited greater creep resistance than Ti-6Al-4V. The greater creep resistance of TCFA alloy could also be due to the presence of $TiCr_2$ phase along with α+ω precipitates in the β-phase matrix. D. Northwood et al, found that the multi-phase Ti-13V-11Cr-3Al (wt.%) alloy with β + α + $TiCr_2$ phases had a slower creep rate in the secondary regime than the single β-phase Ti-13V-11Cr-3Al (wt.%) alloy (Northwood and Smith, 1987).

CHAPTER 4

CONCLUSIONS

1. The as-processed XRD results showed the presence of β-phase peaks. After heat-treatment at 683 K for 12 hrs, the XRD results showed peaks corresponding to α and/or ω secondary phase(s). Post creep tested XRD revealed peaks corresponding to α, ω, and $TiCr_2$ secondary phase(s) for the alloys. The SE SEM images of the creep tested samples revealed nanoscale pit-like structures suggesting the presence of secondary phase(s).

2. TC exhibited the largest grain size while TCFA exhibited the smallest grain size after creep.

3. The addition of Al and Fe did not contribute to a significant change in the Vickers hardness of the as-processed alloys. Post heat-treatment and post creep tested Vickers hardness values for the alloys showed an increase when compared to the as-received material indicating possible phase transformations during the aging process and precipitation hardening effects observed in β-Ti alloys which strongly hinders the movement of dislocations. TCFA exhibited the highest hardness followed by TCA and then TC. A slight increase of about 5%-10% in the hardness values was observed going from the grip to the gage sections of the creep tested alloys which could be the result of the higher dislocation content in the gage section.

4. The creep strain increased as the applied stress was increased from 200 MPa to 350 MPa for all the alloys during creep testing. The creep strength results followed the same trend as the hardness results. TCFA exhibited the greatest creep resistance followed by TCA and then TC at 683 K and for all stress levels. TCFA exhibited greater creep resistance than Ti-6Al-4V after heat treatment at 683 K for 48 hrs prior to creep testing and exhibited lower creep

resistance than Ti-6Al-4V in the no prior heat treatment case.

5. TC and TCA showed similar values of 59.7 % and 59.1 % respectively for the precipitate volume fraction. As such, there seemed to be a reduced effect of Al on the precipitate volume fraction. TCFA had a higher precipitate volume percent of 63.1 %. The addition of Fe and Al to TC exhibited an increase of about 6 % in the precipitate volume percent compared to TC alloy.

Recommendations for future work

1. Determining other mechanical properties like tensile strength, elongation-to-failure, fatigue strength and correlating them with the microstructural changes is crucial in developing an understanding of the influence of alloying elements on properties. Such studies will be important in developing cheaper alternatives to the current Ti alloys commercially being used.

2. To have a better understanding of the creep mechanisms, it is necessary to estimate the activation energies and the creep exponent values of the different mechanisms observed. Future work could focus on performing more creep tests at different creep temperatures to estimate the activation energies which would in turn help understand the deformation mechanisms observed. Also, performing creep tests are more stress levels will help obtain a more accurate creep exponent plot and value.

3. In-situ creep tests for the alloys could be conducted and used to characterize the distribution of the different deformation modes as a function of testing conditions (i.e. stress, temperature and loading rate).

4. To verify the phase(s) observed, future transmission electron microscopy (TEM) analysis,

and EBSD analysis could be conducted.

APPENDIX

APPENDIX

MATLAB code for calculating strain rate

The following Matlab code was used to calculate the strain rate from the deflection and time data collected from the creep test frames and obtain a plot of strain rate vs time.

```
a=importdata('strain_rate.xlsx');
t=a(:,1);
d=a(:,2);
for i=1:2000;
    t1=t(i);
    t2=t(i+50);
    d1=d(i);
    d2=d(i+50);
    v(i)=(d2-d1)/(t2-t1);
end
plot(t(1:2000),v);
```

where ‘t’, ‘d’, ‘t1’, ‘t2’, ‘d1’, ‘d2’, and ‘v’ are variables used for time, deflection, first time value, second time value, first deflection value, second deflection value, strain rate respectively.

Strain rate vs time plots for all alloys at 683 K

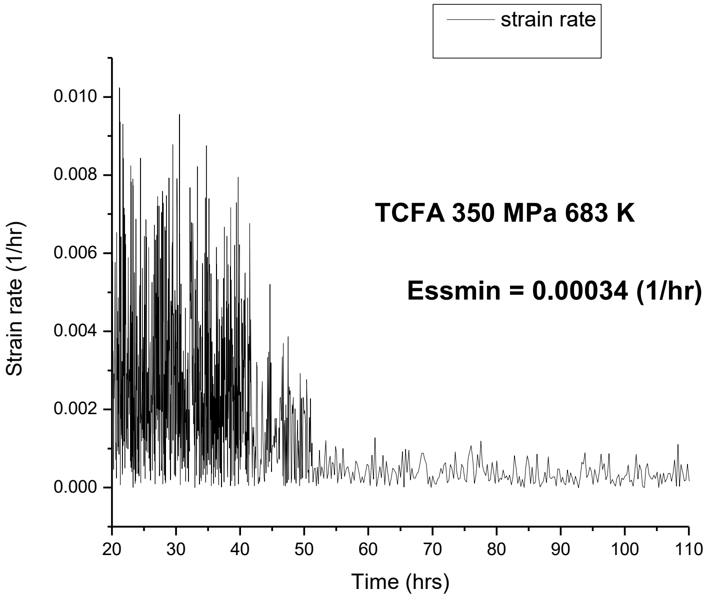

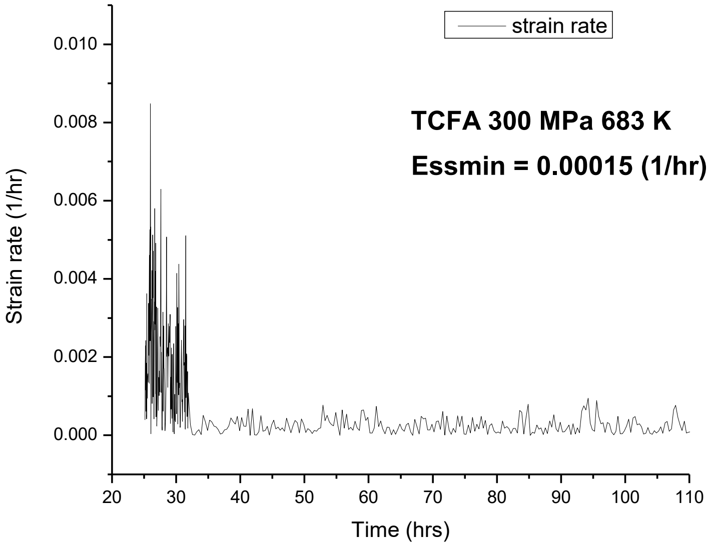

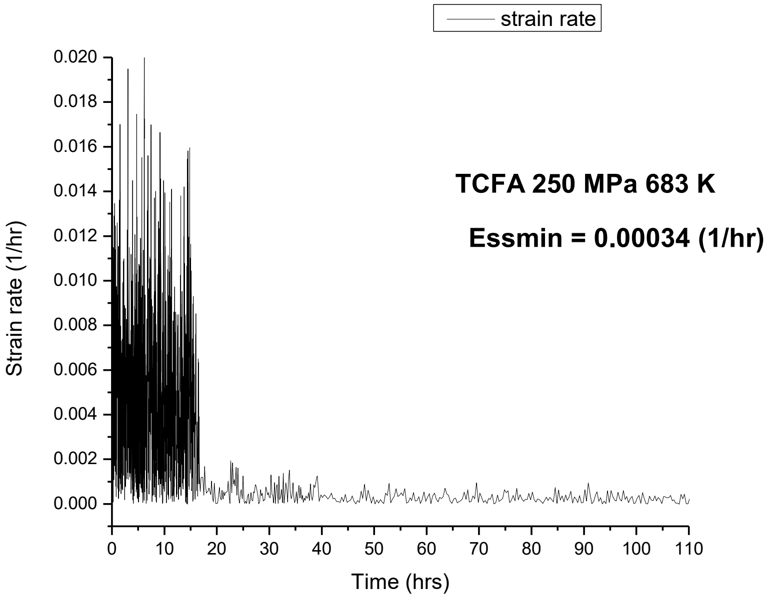
strain rate
TCFA 250 MPa 683 K
Essmin = 0.00034 (1/hr)
Strain rate (1/hr)
0.020
0.018
0.016
0.014
0.012
0.010
0.008
0.006
0.004
0.002
0.000
Time (hrs)
0
10
20
30
40
50
60
70
80
90
100
110

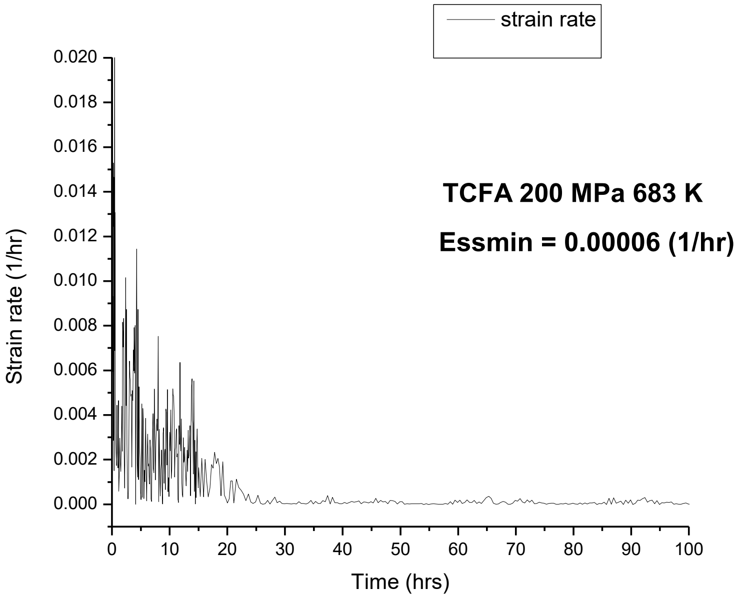
strain rate
TCFA 200 MPa 683 K
Essmin = 0.00006 (1/hr)
Strain rate (1/hr)
0.020
0.018
0.016
0.014
0.012
0.010
0.008
0.006
0.004
0.002
0.000
Time (hrs)
0
10
20
30
40
50
60
70
80
90
100

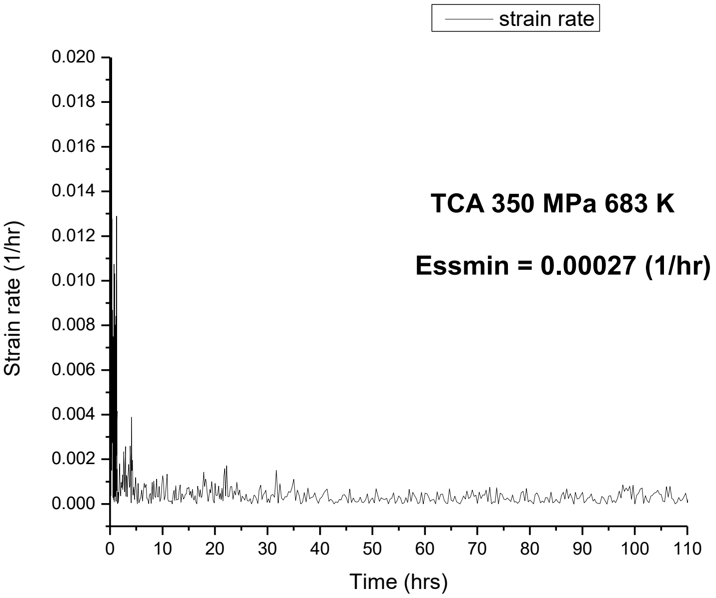
strain rate
TCA 350 MPa 683 K
Essmin = 0.00027 (1/hr)
Strain rate (1/hr)
0.020
0.018
0.016
0.014
0.012
0.010
0.008
0.006
0.004
0.002
0.000
0
10
20
30
40
50
60
70
80
90
100
110
Time (hrs)

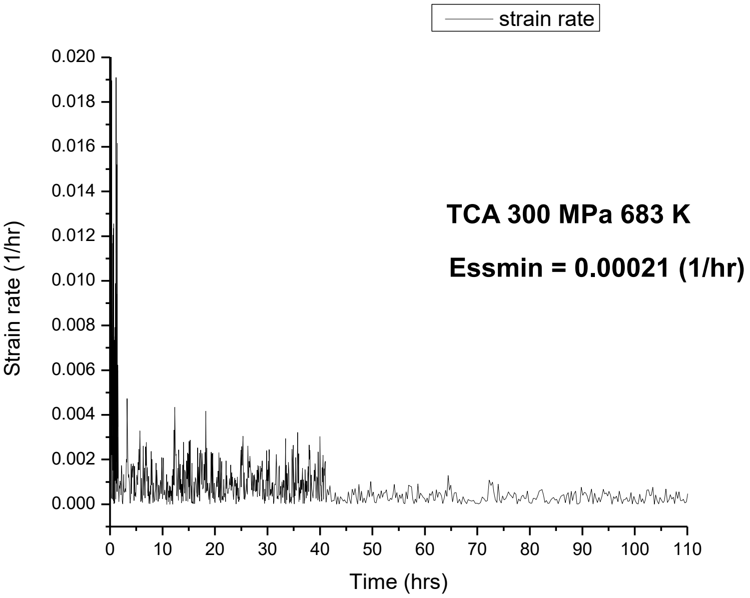
strain rate
TCA 300 MPa 683 K
Essmin = 0.00021 (1/hr)
Strain rate (1/hr)
0.020
0.018
0.016
0.014
0.012
0.010
0.008
0.006
0.004
0.002
0.000
0
10
20
30
40
50
60
70
80
90
100
110
Time (hrs)

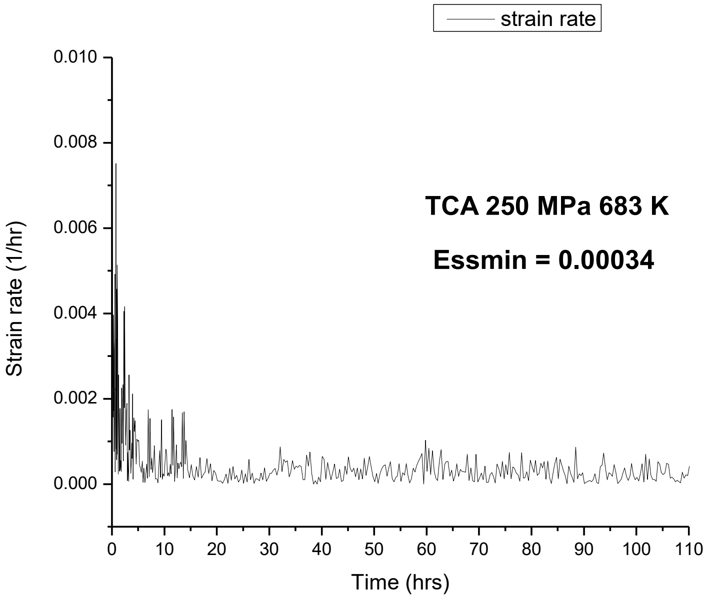
strain rate
TCA 250 MPa 683 K
Essmin = 0.00034
Strain rate (1/hr)
0.010
0.008
0.006
0.004
0.002
0.000
Time (hrs)
0
10
20
30
40
50
60
70
80
90
100
110

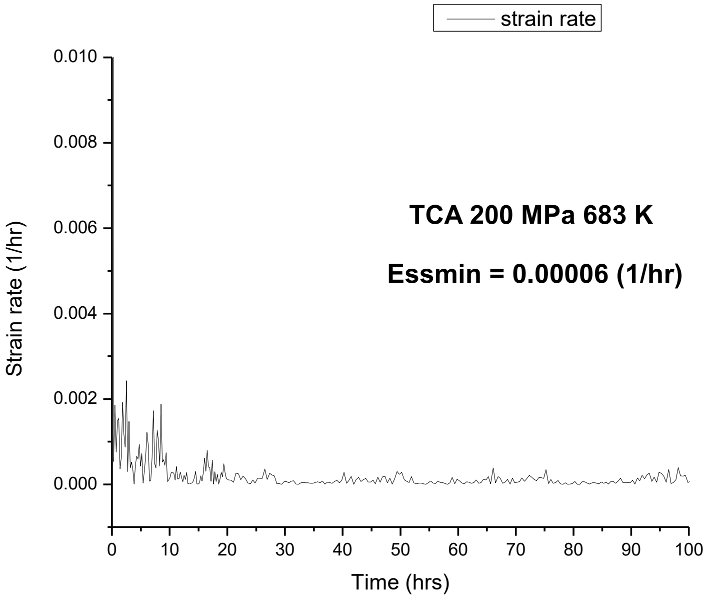
strain rate
TCA 200 MPa 683 K
Essmin = 0.00006 (1/hr)
Strain rate (1/hr)
0.010
0.008
0.006
0.004
0.002
0.000
Time (hrs)
0
10
20
30
40
50
60
70
80
90
100

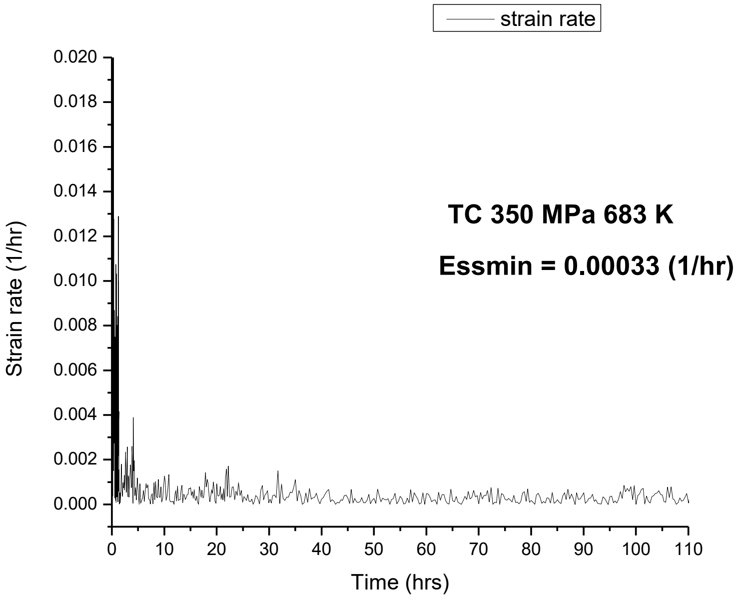
strain rate
TC 350 MPa 683 K
Essmin = 0.00033 (1/hr)
Strain rate (1/hr)
0.020
0.018
0.016
0.014
0.012
0.010
0.008
0.006
0.004
0.002
0.000
0
10
20
30
40
50
60
70
80
90
100
110
Time (hrs)

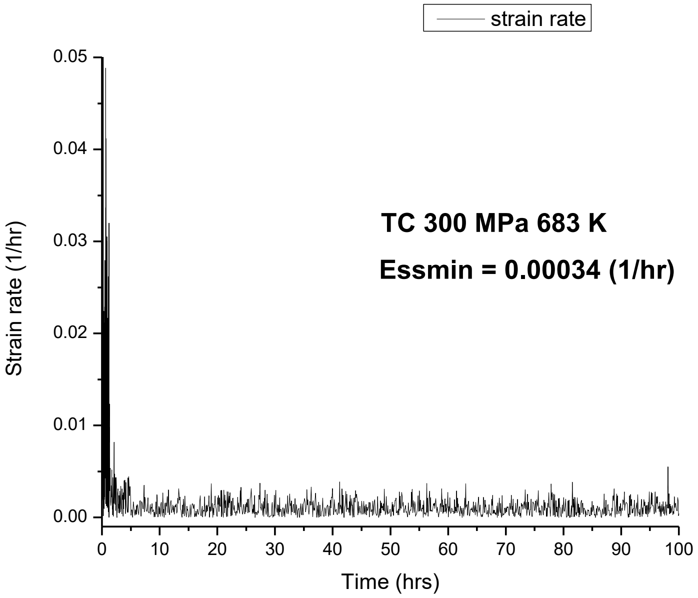
strain rate
TC 300 MPa 683 K
Essmin = 0.00034 (1/hr)
Strain rate (1/hr)
0.05
0.04
0.03
0.02
0.01
0.00
0
10
20
30
40
50
60
70
80
90
100
Time (hrs)

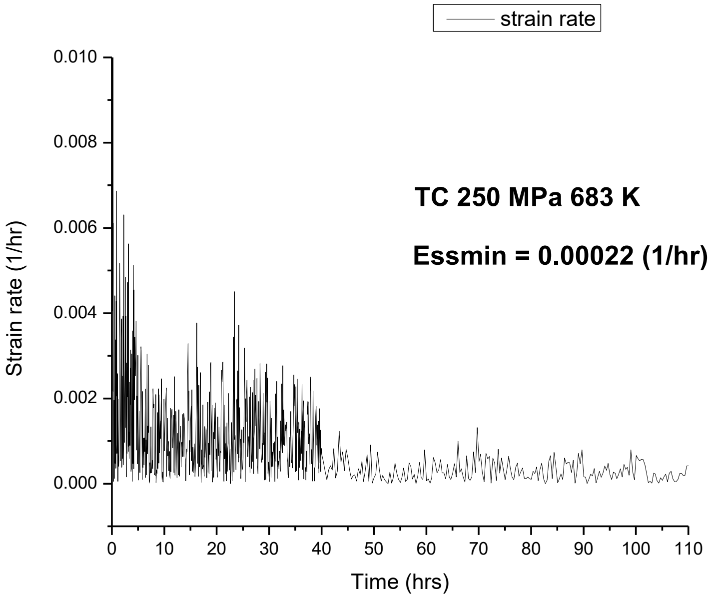
strain rate
0.010
0.008
0.006
0.004
0.002
0.000
Strain rate (1/hr)
TC 250 MPa 683 K
Essmin = 0.00022 (1/hr)
0
10
20
30
40
50
60
70
80
90
100
110
Time (hrs)

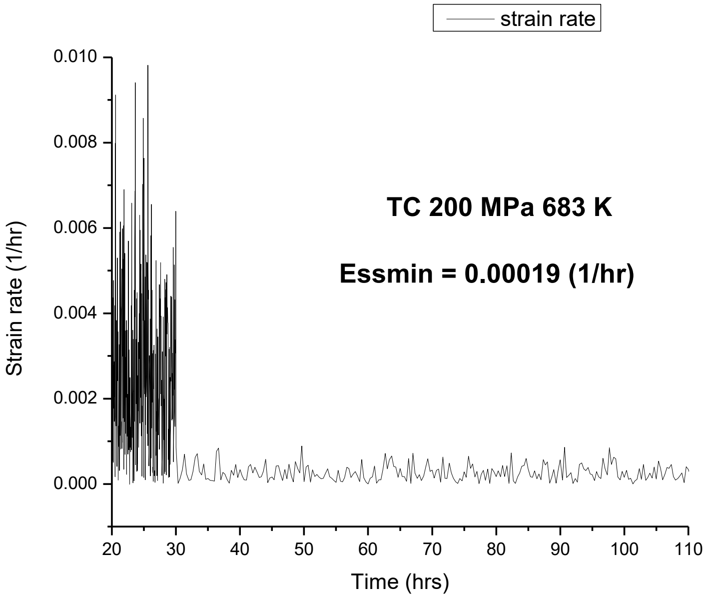
strain rate
0.010
0.008
0.006
0.004
0.002
0.000
Strain rate (1/hr)
TC 200 MPa 683 K
Essmin = 0.00019 (1/hr)
20
30
40
50
60
70
80
90
100
110
Time (hrs)

BIBLIOGRAPHY

BIBLIOGRAPHY

Ankem, S. and Greene, C. . (2002) ‘Recent developments in microstructure/property relationships of beta titanium alloys’, *Materials Science and Engineering: A*, 263(2), pp. 127–131. doi: 10.1016/s0921-5093(98)01170-8.

ASTM E92-17 (2017) ‘No TitleStandard Test Methods for Vickers Hardness and Knoop Hardness of Metallic Materials’, *ASTM International, West Conshohocken, PA*.

Azimzadeh, S. and Rack, H. J. (1998) ‘Phase transformations in Ti-6.8 Mo-4.5 Fe-1.5 Al’, *Metallurgical and Materials Transactions A*. Springer, 29(10), pp. 2455–2467.

Ballor, J *et al.* (2019) ‘Composition-Dependent Microstructure-Property Relationships of Fe and Al Modified Ti-12Cr (wt.%)’, *JOM*. Springer, pp. 1–10.

Banerjee, R. *et al.* (2004) *Strengthening mechanisms in {Ti}–Nb–Zr–Ta and {Ti}–Mo–Zr–Fe orthopaedic alloys*. Biomaterials 25, 3413–3419.

Barrett, C. S. (1966) ‘TB Massalski Structure of Metals’. McGraw-Hill, New York.

Boyer, R., Welsch, G. and Collings, E. (1994) *editors*. Materials Park, OH: ASM International.

Chen, K. C. (1996) *Compositional influences on the microstructures, phase stability, and mechanical properties of* $TiCr_2$ *laves phase alloys*. Available at: http://hdl.handle.net/1721.1/40213.

Chen, Y. *et al.* (2014) ‘Effect of aging heat treatment on microstructure and tensile properties of a new β high strength titanium alloy’, *Journal of Alloys and Compounds*. Elsevier, 586, pp. 588–592.

Chunxiang, C. *et al.* (2003) ‘Fabrication and Bio-compatibility of K~ 2Ti~ 6O~ 1~ 3 Bio-ceramic Coating on the Surface of the Titanium Alloy TiAl~ xZr~ x~-~ 4Sn~ x~-~ 3~.~ 5Nb~ x~-~ 4~.~ 5’, *Rare Metal Materials and Engineering*. SCIENCE PRESS, 32(8; ISSU 205), pp. 627–630.

Chunxiang, C. *et al.* (2011) ‘Titanium alloy production technology , market prospects and industry development Titanium alloy production technology , market prospects and industry development’, *Materials and Design*. Elsevier Ltd, 32(3), pp. 1684–1691. doi: 10.1016/j.matdes.2010.09.011.

Clementi, E., Raimondi, E. and Reinhardt, P. (1963) ‘Atomic screening constants from SCF functions’, *The Journal of Chemical Physics*, 38(11), pp. 2686–2689.

Coble, R. L. (1963) ‘A model for boundary diffusion controlled creep in polycrystalline materials’, *Journal of applied physics*. AIP, 34(6), pp. 1679–1682.

Cotton, J. D. *et al.* (2015) ‘State of the art in beta titanium alloys for airframe applications’, *Jom*. Springer, 67(6), pp. 1281–1303.

Cullity, B. D. and Stock, S. R. (2001) *Elements of X-ray Diffraction*. Prentice hall New Jersey.

D., J. W. and A., W. W. (1968) 'Creep rupture properties of {Ti}-8Al-1Mo-1V alloy', *Journal of Research of the National Bureau of Standards-C. Engineering and Instrumentation, Vol. 72C, No,* 72C(2).

Dehghan-Manshadi, A. and Dippenaar, R. J. (2011) 'Development of α-phase morphologies during low temperature isothermal heat treatment of a Ti--5Al--5Mo--5V--3Cr alloy', *Materials Science and Engineering: A*. Elsevier, 528(3), pp. 1833–1839.

Donachie, M. J. (2000) *Titanium: a technical guide*. ASM international.

Dubinskiy, S. *et al.* (2016) 'In situ X-ray diffraction study of athermal and isothermal omega-phase crystal lattice in Ti-Nb-based shape memory alloys', *Materials Letters*. Elsevier, 168, pp. 155–157.

Evans, R. W. and Wilshire, B. (1985) *Creep of metals and alloys*. London : Institute of Metals.

Flegler S.L., Heckman J.W.Jr., and K. K. L. (1993) *Scanning and Transmission Electron Micrscopy: An Introduction, W.H.Freeman, New York*.

Gollapudi, S., Charit, I. and Murty K, L. (2008) 'Creep mechanisms in {Ti}–3Al–2', *5 {V} alloy tubing deformed under closed-end internal gas pressurization, {Acta} {Materialia}*, 56(10), pp. 2406–2419.

Gunawarman, B. *et al.* (2005) 'Mechanical properties and microstructures of low cost β titanium alloys for healthcare applications', *Materials Science and Engineering: C*. Elsevier, 25(3), pp. 304–311.

Hariharan, V. S. (2018) 'Phase fraction calculation of microstructure using ImageJ'. doi: 10.13140/RG.2.2.22990.51521.

Hayes R, W., Vishwanathan G, B. and Mills M, J. (2002) 'Creep behavior of {Ti}–6Al–2Sn–4Zr–2Mo: {I}', *The effect of nickel on creep deformation and microstructure, {Acta} {Materialia}*, 50, pp. 4953–4963.

Herring, C. (1950) 'Diffusional viscosity of a polycrystalline solid', *Journal of applied physics*. AIP, 21(5), pp. 437–445.

Hickman, B. S. (1969) 'The formation of omega phase in titanium and zirconium alloys: A review', *Journal of Materials Science*. Springer, 4(6), pp. 554–563.

Ikeda, M. *et al.* (2004) 'The effect of cooling rate from solution treatment temperature on phase constitution and tensile properties of Ti-4.3 Fe-7.1 Cr-3.0 Al alloy', *Materials transactions*. The Japan Institute of Metals and Materials, 45(5), pp. 1566–1570.

Ivasishin, O. M. *et al.* (2003) 'Precipitation and recrystallization behavior of beta titanium alloys during continuous heat treatment', *Metallurgical and Materials Transactions A*. Springer, 34(1), pp. 147–158.

Ivasyshyn, O. M. and Aleksandrov, A. V (2008) 'Status of the titanium production, research, and applications in the CIS', *Materials Science*. Springer, 44(3), pp. 311–327.

Joshi, V. A. (2006) *Titanium alloys: an atlas of structures and fracture features*. Crc Press.

Khademi, V. (2018) 'An Experimental-Computational Study on the Plastic Deformation Behavior of Body-Centered Cubic Titanium Alloys'.

Kobayashi, E. *et al.* (1998) 'Influence of aging heat treatment on mechanical properties of biomedical Ti--Zr based ternary alloys containing niobium', *Journal of Materials Science: Materials in Medicine*. Springer, 9(11), pp. 625–630.

Kolli, R. P., Joost, W. J. and Ankem, S. (2015) 'Phase stability and stress-induced transformations in beta titanium alloys', *Jom*. Springer, 67(6), pp. 1273–1280.

Kuan, T. S., Ahrens, R. R. and Sass, S. L. (1975) 'The stress-induced omega phase transformation in Ti-V alloys', *Metallurgical Transactions A*. Springer, 6(9), p. 1767.

Lee, C. M., Ju, C. P. and Lin, C. (2002) 'J', *H. (2002). {Structure}-property relationship of cast {Ti}-{Nb} alloys. {J} {Oral} {Rehabil}*, 29.

Leyens, C. and Peters, M. (2003a) *Edited by Handbook of Cellular Metals Phase Transformations in Materials*.

Leyens, C. and Peters, M. (2003b) *Titanium and Titanium Alloys, Fundamentals and Applications*. Wiley–VCH {GmbH} & Co.

Leyens, C. and Peters, M. (2006) *Titanium and Titanium Alloys: Fundamentals and Applications (John Wiley & Sons)*.

Li, S. *et al.* (2002) 'Effect of Nb on microstructural characteristics of Ti-Nb-Ta-Zr alloy for biomedical applications', *Materials transactions*. The Japan Institute of Metals and Materials, 43(12), pp. 2964–2969.

Li, T. *et al.* (2015) 'The mechanism of ω-assisted α phase formation in near β-Ti alloys', *Scripta Materialia*. Elsevier, 104, pp. 75–78.

Liu, B. *et al.* (2008) 'TITANIUM 2008: development of international titanium industry, preparation technology and applications', *Mater Sci Eng Pow Metall*, 14(2), pp. 67–73.

Liu, Z. and Welsch, G. (1988) *Effects of oxygen and heat treatment on the mechanical properties of alpha and beta titanium alloys*. MTA 19, 527–542.

Lütjering, G., and Williams, J. C. (2003) 'Titanium', *Berlin Heidelberg: Springer-Verlag*.

Lütjering, Gerd and Williams, J. C. (2003) 'Commercially Pure (CP) Titanium and Alpha Alloys', in *Titanium*. Springer, pp. 149–175.

Martin, B. W. (2017) *Development of a novel , bicombinatorial approach to alloy development , and application to rapid screening of creep resistant titanium alloys*.

Massalski, T. B. (1990) ‘Binary Alloy Phase Diagrams vol 1 (Ohio: ASM International, Materials Park)’.

Metallurgy, D. G. E. M. (1986) *3rd ed.* New York: {McGraw}-Hill.

Nabarro, F. R. N. (1948) ‘Report of a Conference on the Strength of Solids’, *The Physical Society, London*, 75.

Nag, S. *et al.* (2009a) ‘ω-{Assisted} nucleation and growth of α precipitates in the {Ti}–5Al–5Mo–5V–3Cr–0’, *5Fe β titanium alloy. {Acta} {Materialia}*, 57.

Nag, S. *et al.* (2009b) ‘ω-Assisted nucleation and growth of α precipitates in the Ti--5Al--5Mo--5V--3Cr--0.5 Fe β titanium alloy’, *Acta Materialia*. Elsevier, 57(7), pp. 2136–2147.

Niinomi, M. (2008) *Mechanical biocompatibilities of titanium alloys for biomedical applications*. Journal of the Mechanical Behavior of Biomedical Materials 1, 30–42.

Northwood, D. O. and Smith, I. O. (1987) ‘Effect of metallurgical condition on the creep behaviour of Ti-13V-11Cr-3Al’, *Journal of materials science letters*. Springer, 6(7), pp. 820–822.

Ogawa, M. *et al.* (2007) ‘The Effect of Al Content on Tensile and Fatigue Properties of Solution-Treated and Quenched Ti-13Cr-1Fe Alloys’, *Mater. Trans*, 48.

Ogawa, M. *et al.* (2008) ‘Effect of Cooling Rate on Mechanical Properties of Ti-13 Cr-1 Fe-3 Al Alloy’, *Journal of the Japan Institute of Metals*. Japan Institute of Metals, Nihon Kinzoku Gakkai Aoba, Aramaki Sendai 980 Japan, 72(12), pp. 983–988.

Ohmori, Y. *et al.* (2001) ‘Effects of ω-phase precipitation on β → α, α″ transformations in a metastable β titanium alloy’, *Materials Science and Engineering: A*. Elsevier, 312(1–2), pp. 182–188.

P. Ganesan, R. J. D. and G. A. S. (1974) ‘The effect of heat treatment on the mechanical properties and Young’s modulus of beta titanium alloys’, 34, pp. 209–214.

Pennock, G. M., Flower, H. M. and West, D. R. F. (1980) ‘Titanium’80 Sci’. Technol.

Perez-Prado, M. T. and Kassner, M. E. (2015) *The 3-Power-Law Viscous Glide Creep*. Third Edit, *Fundamentals of Creep in Metals and Alloys: Third Edition*. Third Edit. Elsevier Ltd. doi: 10.1016/B978-0-08-099427-7.00005-0.

Prima, F. *et al.* (2006) ‘Evidence of α-nanophase heterogeneous nucleation fromω particles in a β-metastable Ti-based alloy by high-resolution electron microscopy’, *Scripta materialia*. Elsevier, 54(4), pp. 645–648.

Qazi, J. I. *et al.* (2005) ‘Effect of Aging Treatments on the Tensile Properties of Ti-35Nb-7Zr-5Ta-

(0.06--0.7) O Alloys', *Journal of ASTM International*. ASTM International, 2(8), pp. 1–19.

Rhodes, C. G. and Williams, J. C. (1975) *Precipitation of alpha phase in metastable beta phase titanium alloys. Technical report.[Ti-Mo and Ti-Mo-Al]*.

Samimi, P. *et al.* (2015) 'A new combinatorial approach to assess the influence of alloy composition on the oxidation behavior and concurrent oxygen-induced phase transformations for binary Ti--xCr alloys at 650 C', *Corrosion Science*. Elsevier, 97, pp. 150–160.

Sherby, O. D., Anderson, R. A. and Dorn, J. E. (1951) 'Effect of alloying elements on the elevated temperature plastic properties of alpha solid solutions of aluminum', *JOM*. Springer, 3(8), pp. 643–652.

Sugano, D. and Ikeda, M. (2005) 'The effect of aluminum content on phase constitution and heat treatment behavior of Ti--Cr--Al alloys for healthcare application', *Materials Science and Engineering: C*. Elsevier, 25(3), pp. 377–381.

Takashi Maeda (1988) *Phase Equilibrium and Beta Stability in Ti-Rich Ti-V-Al Alloys*.

'Test Methods for Determining Average Grain Size' (2010) *ASTM International*.

Welsch, G., Boyer, R. and Collings, E. W. (1993) *Materials Properties Handbook: Titanium Alloys ({ASM} International).*

Williams, J. C. and Blackburn, M. J. (1969) *The influence of misfit on the morphology and stability of the omega phase in titanium--transition metal alloys.*

Wilshire, B. and Owen, D. R. J. (1981) *Creep and Fracture of Engineering Materials and Structures: Proceedings of the International Conference Held at University College, Swansea, 24th-27th March, 1981*. Pineridge Press.